Flying into the Cold: First Results from the NSF Cold-Air outbreak Experiment in the Sub-ARctic (CAESAR)

Paquita Zuidema[a] , Bart Geerts[b] , Greg McFarquhar[c] , Adriana Bailey[d] , John Cassano[e] , James Doyle[f] , Jeffrey French[b] , Russell Perkins[g] , Markus Petters[h] , Jefferson R. Snider[b] , Yonggang Wang[i] , Zhien Wang[j] , Lintong Cai[h] , Robert David[s] , Paul J. DeMott[g] , Andrew Dzambo[c] , Coltin Grasmick[b] , Emma Järvinen[l] , Pavel Romashkin[k] , Elise Rosky[d,k] , Carol Ruchti[k] , Michael Tjernström[q] , Peisang Tsai[k] , Patrick Veres[k] , Holger Vömel[k] , Sarah Woods[k] , Cory Wolff[k] , Daniel Zietlow[k] , John Allison[k] , Nick Amundsen[c] , Janine Aquino[k] , Clayton Arendt[k] , Aaron Bansemer[k] , Eric Beamesderfer[b] , Ezekiel Caldon[i] , Teresa Campos[k] , Tim Carlsen[s] , Bo Chen[g] , Owen Cruikshank[b] , Catherine Dewerd[k] , Gregory Elsaesser[t] , Samuel Ephraim[a] , Mack Goodstein[k] , Sarah Gryskewicz[i] , Julie Haggerty[k] , Justin Hicks[k] , Yongjie Huang[c] , Timothy Juliano[k] , Natalie Kille[b] , Sonia Kreidenweis[g] , Chris Kruse[k] , Bee Lamsma[i] , Scot Loehrer[k] , Genevieve Lorenzo[a] , Sunandan Mahant[h] , Adam Majewski[b] , Shane Martrich[b] , Camille Mavis[g] , Flynn McGinnity[j] , Evy McUmber[k] , Evan Newman[b] , Qing Niu[c] , Louis Nguyen[m] , Gunnar Noer[n] , Saurabh Patil[c] , Ryan Patnaude[g] , Erika Pruitt[c] , Josephine Ragland[j] , Michael Reeves[k] , Amanda Richter[c] , Anna Robertson[b] , Franziska Rogge[o] , Mampi Sarkar[u] , Martin Schnaiter[l] , Andrew Seidl[p] , Harald Sodemann[p] , Gunilla Svensson[q] , William Smith[m] , Susan Stringer[k] , Tyler Tatro[a] , Florian Tornow[r] , Pablo Velt[b] , Emma Weissburg[b] , Jingbo Wu[r] , Lulin Xue[k] , Zeqian Xia[c]

[a] *Dept. of Atmospheric Sciences, Rosenstiel School, U of Miami, Miami, FL USA* [b] *University of Wyoming, Laramie, WY, USA* [c] *Cooperative Institute for Severe and High-Impact Weather Research and Operations and University of Oklahoma, Norman, OK, USA* [d] *University of Michigan, Ann Arbor, MI, USA* [e] *University of Colorado-Boulder, Boulder, CO, USA* [f] *Naval Research Laboratory, Monterey, CA, USA* [g] *Colorado State University, Ft. Collins, CO USA* [h] *University of California at Riverside, Riverside, CA USA* [i] *State University of New York at Oswego, Oswego, NY USA* [j] *State University of New York at Stonybrook, Stonybrook, NY USA* [k] *NSF National Center for Atmospheric Research, Boulder, CO USA* [l] *Institute for Atmospheric*

Early Online Release: This preliminary version has been accepted for publication in *Bulletin of the American Meteorological Society*, may be fully cited, and has been assigned DOI 10.1175/BAMS-D-25-0241.1. The final typeset copyedited article will replace the EOR at the above DOI when it is published.

and Environmental Research, University of Wuppertal, Wuppertal, Germany [m] *NASA Langley Research Center, Hampton, VA, USA* [n] *Met Norway, Bergen, Norway* [o] *Karlsruhe Institute of Technology, Karlsruhe, Germany* [p] *University of Bergen, Bergen, Norway* [q] *Stockholm University, Stockholm, Sweden* [r] *Center for Climate Systems Research, Columbia University, New York, NY, USA and Goddard Institute for Space Studies, NASA, New York, NY, USA* [s] *University of Oslo, Oslo, Norway* [t] *Goddard Institute for Space Studies, Dept. of Applied Physics and Applied Mathematics, Columbia University and NASA, New York, NY, USA* [u] *Rice University, Houston, TX, USA*

Corresponding author: P. Zuidema, pzuidema@miami.edu

T. Juliano current affiliation: AiDASH, Palo Alto, CA

E. McUmber current affiliation: University of Colorado-Boulder, Boulder, CO

R. Patnaude current affiliation: NSF NCAR, Boulder, CO

Accepted for publication in *Bulletin of the American Meteorological Society.* DOI 10.1175/BAMS-D-25-0241.1.

ABSTRACT: The National Science Foundation-sponsored Cold-Air outbreak Experiment over the Sub-Arctic Region (CAESAR) is motivated by hypotheses in how dynamical, aerosol and cloud microphysical processes influence cold-air outbreak development and the accompanying spatial organization of clouds and precipitation, including in polar lows. CAESAR characterized the aerosol, thermodynamic and dynamic environment occupied by mixed-phase clouds within air masses moving southward off the Arctic sea ice over the Greenland/Norwegian Seas in the spring of 2024. The aircraft campaign supported a suite of remote sensing and in situ measurements below, within and above the mostly shallow convective clouds. Three flights reached the Greenland Marginal Ice Zone. A golden-case cold-air outbreak, sampled from its origin in clear skies over 100% sea ice, revealed a boundary layer containing anthropogenically-modified air, with the first-detected in situ cloud particles being ice polycrystals, within -25 °C air. Two flights sampled polar lows, and another flight characterized a closed-to-open cell transition occurring under high aerosol loading originating from Siberia and strong surface fluxes. The transition occurred after drizzle-sized drops developed within a boundary layer deepening under a weakening inversion. Combined ice particle and ice nucleating particle concentrations suggest most ice production is primary at cloud temperatures < -20 °C, with secondary ice production evident at cloud temperatures > -20 °C. Overall these first observations already reveal a diversity of CAO cloud structures.

Accepted for publication in *Bulletin of the American Meteorological Society.* DOI 10.1175/BAMS-D-25-0241.1.

SIGNIFICANCE STATEMENT: Winter Arctic air plunging south brings frigid air and snowfall and disrupts social and economic networks. The outbreaks of cold air moving over open water sustain high winds, with extreme surface fluxes of heat and moisture able to spawn intense polar lows. How such events will change in the future remains difficult to predict. To address this research gap, comprehensive CAESAR measurements promote in-depth investigation into the wide ranges of relevant process scales, from turbulence and microphysics to synoptics. The observations increase our understanding of a common cloud regime that is an integral component of the Arctic climate. This understanding will ultimately yield economic benefits and increased social stability by improving Arctic weather prediction at all time scales.

CAPSULE: Observations of mixed-phase cloudy cold-air outbreak clouds over the Nordic Seas explore the complexities of a common weather regime impactful at many time scales to commerce and coastal communities.

1. Introduction

When cold, dry Arctic air passes over open water, strong winds encourage extreme fluxes of moisture, heat and sea-spray into the environment. These synoptic events support complex aerosol-cloud-precipitation interactions that involve both super-cooled liquid and ice, cloud condensation nuclei (CCN) and ice-nucleating particle (INP) concentrations, and strong turbulence driven by both buoyancy and wind shear. These processes support evolving cloud morphologies composed of cloud streets, closed- and open-celled convective structures of varying aspect ratios, impacting the surface radiative budget and at times becoming polar lows. The modeling and prediction challenges stemming from the coupled microphysical, turbulence and radiative processes span a wide range of temporal and spatial scales (Chechin and Pichugin 2015; Juliano et al. 2024; Screen et al. 2025; Huang et al. 2025; Juliano et al. 2026). The most intense cold-air outbreaks (CAOs) occur over the Greenland and Barents Seas (Mateling et al. 2023). The CAO cloud genesis begins over the marginal ice zone (MIZ): the transitional zone between open sea and dense drift ice, spanning between 15% to 80% sea ice coverage (Dumont 2022). Over the Greenland Sea, 60% to 80% of the wintertime oceanic heat loss (Papritz and Spengler 2017; Smedsrud et al. 2022) occurs during CAOs, coincident with a global maximum in large-scale ocean evaporation events (Aemisegger and Papritz 2018). Changes in global circulation may support increases in wintertime CAOs in some

Accepted for publication in *Bulletin of the American Meteorological Society.* DOI 10.1175/BAMS-D-25-0241.1.

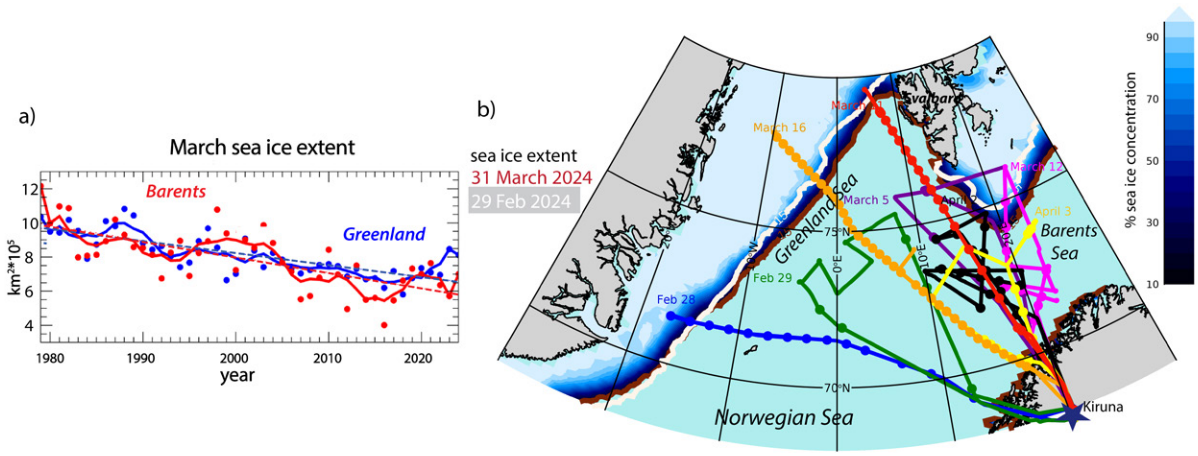

Fig. 1. a) Yearly March-mean sea ice extents for Greenland Sea (blue) and Barents Sea (red) from 1979 through 2024, with best-fit trends indicated (dashed lines). The marginal ice zones of the two seas are distinguished at the southern tip of Svalbard. b) Sea ice concentrations for 31 March 2024 (white-blue scale) with sea ice extents (sea ice concentrations > 15%) indicated for 31 March 2024 (thick maroon line) and 28 February 2024 (off-white line). CAESAR flight tracks colored by date (28 Feb-blue, 29 Feb-green, 5 March-purple, 11 March-red, 12 March-pink, 16 March-orange, 2 April-black and 3 April-yellow). Dropsonde locations indicated (filled circles).

'locked-in' locations that include the eastern US seaboard and Europe (Kornhuber and Messori 2023). Here, more CAOs can mean more severe winters (Hartmuth et al. 2024). Although overall CAOs are expected to decrease in intensity as the Arctic warms (Serreze et al. 2009; Dahlke et al. 2022; Rantanen et al. 2022), wintertime CAOs have increased over the Nordic Seas in the past 25 years (von der Lippe et al. 2026).

The month with the largest Arctic sea ice extent is March (Onarheim et al. 2018). Since 1979, sea ice coverage in the North Atlantic has decreased during March (Fig. 1a). The Greenland and Barents Seas (their domains are separated at the southern end of Svalbard) have lost 19% and 26% of their March sea ice extent since 1979 relative to the 1979-2024 mean (Fig. 1a), although the statistical significance remains debated (England et al. 2025). The Odden ice tongue, a key wintertime sea ice formation region, is no longer present to the northeast of Jan Mayen island (71°N, 8.5°W) (Comiso et al. 2001). The coastal sea temperatures of the North Atlantic Current tongue reaching Norway are also increasing over time (Baumann et al. 2025). At decadal time scales, the reduction in sea ice is strongly implicated in Arctic warming, which maximizes at the

Accepted for publication in *Bulletin of the American Meteorological Society*. DOI 10.1175/BAMS-D-25-0241.1.

Table 1. Recent significant campaigns with a focus on convective marine mixed-phase clouds.

Campaign	Base	Location	Time Span	CAO-relevant references (when available)
Northern Latitudes:				
ARCSIX	aircraft	N of Greenland	summer 2024	–
HALO-AC^3	aircraft	Greenland Sea	spring 2022	Schirmacher et al. (2024), Wendisch et al. (2025)
ACAO	aircraft	near Svalbard	spring 2022	Raif et al. (2024), Clarke et al. (2026)
M-PHASE	aircraft	Labrador Sea	October 2022	Huang et al. (2025), Biggart et al. (2026)
ACTIVATE	aircraft	NW Atlantic	2020-2022	Seethala et al. (2024), Tornow et al. (2025b) Pearson et al. (2026)
ACLOUD+PASCAL	aircraft+ship	near Svalbard	May-June 2017	Knudsen et al. (2018)
ACCACIA	aircraft	near Svalbard	spring, summer 2013	Abel et al. (2017)
M-PACE	aircraft	Beaufort Sea	autumn 2005	Solomon et al. (2009), Fu et al. (2019)
ARKTIS	aircraft	Greenland Sea	1991, 1993	Brümmer (1999)
NSA	surface	northern Alaska	2004-present	de Boer et al. (2011), Wang et al. (2016)
COMBLE	surface	north Norway	spring 2020	Geerts et al. (2022), Lackner et al. (2023a,b), Mages et al. (2023), Juliano et al. (2024), Xia and McFarquhar (2024), Williams et al. (2024), Wu et al. (2025), Juliano et al. (2026)
ISLAS	surface	north Norway	spring 2020,2021,2022	Seidl et al. (2026), Dekhtyareva et al. (2026)
NASCENT	surface	Svalbard	Sept 2019-Aug 2020	Pasquier et al. (2022),Schäfer et al. (2024)
MOSAiC	ship	central Arctic	2019-2020	Kirbus et al. (2023), DeMott et al. (2025)
Southern Latitudes:				
SOCRATES	aircraft	Southern Oceans	Jan-Feb 2018	McFarquhar et al. (2021)
SOC	aircraft	off of Antarctica	Feb 2023	Smith et al. (2025)
MICRE	surface	MacQuarie Island	2016-2018	Tansey et al. (2023)
CAPE-k	surface	Tasmania	April 2024-Sept 2025	-
CAPRICORN I,II	ship	Southern Oceans	March-April 2016, Jan-Feb 2018	Mace et al. (2021)
MARCUS	ship	Southern Oceans	Oct 2017-March 2018	Alexander et al. (2021), Hu et al. (2023)

surface (Screen and Simmonds 2010; Screen et al. 2025). The prospect of a more ice-free Arctic is increasing interest in Arctic shipping (Rodrıguez et al. 2024). At synoptic time scales, the longer fetch over warmer, more ice-free water may also allow CAOs to accumulate more moisture, increasing coastal snowfall (Bailey et al. 2021). Better prediction of Arctic weather has economic benefits, but relating large-scale Arctic change to local precipitation and temperature variability is not trivial.

The National Science Foundation's Cold-Air outbreak Experiment in the Sub-Arctic Region (CAESAR) is motivated by the drive to better understand the properties of Arctic marine CAOs, towards ultimately improving the realism of models used to predict their future behavior. Satellite-based analyses suggest CAOs are more likely to be mixed-phase than non-CAO clouds for a given cloud top temperature (Murray-Watson and Gryspeerdt 2024), with the causes difficult to discern from satellite alone. The causes nevertheless feedback to cloud organization (McCoy et al. 2017)

Accepted for publication in *Bulletin of the American Meteorological Society.* DOI 10.1175/BAMS-D-25-0241.1.

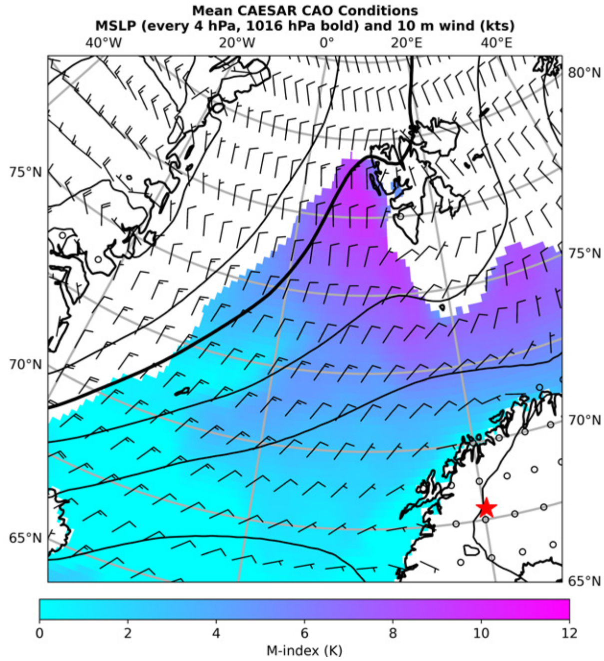

Fig. 2. 83% of the campaign days (30 out of 36 days) contain cloudy cold-air outbreaks reachable by the aircraft, as defined in-field by the forecasting team. ERA5 mean sea level pressure (black contours every 4 hPa, with 1016 hPa contour in bold), mean 950 hPa winds and M-index ($\theta_{surface}$-θ_{850hPa}, in colors, where θ is potential temperature) shown for these 30 days. ERA5-determined 15% sea ice concentrations or greater indicated by the lack of an M-index. The red star denotes Kiruna, Sweden.

and the global radiative balance in a carbon-dioxide-enhanced world (Tan and Storelvmo 2019; Terai et al. 2019), bringing weather-climate connections full circle.

Aircraft campaigns are necessary for gathering measurements on atmospheric vertical structure. A literature review indicates little sampling of the entire cloud and precipitation column for a full CAO lifecyle with both remote sensors and in situ sensors (Table 1). CAESAR provides comprehensive airborne characterization of select CAOs, augmenting the previous surface-based Cold-Air Outbreaks in the Marine Boundary Layer Experiment (COMBLE) campaign based on the Norwegian coast and islands (Geerts et al. 2022; Lackner et al. 2023a,b; Mages et al. 2023), and recent European aircraft campaigns (Abel et al. 2017; Field et al. 2017; Raif et al. 2024; Schirmacher et al. 2024; Wendisch et al. 2025). The CAESAR campaign did not include a dedicated separate modeling component, but ongoing efforts are preparing the datasets to ease their incorporation into process studies.

Accepted for publication in *Bulletin of the American Meteorological Society*. DOI 10.1175/BAMS-D-25-0241.1.

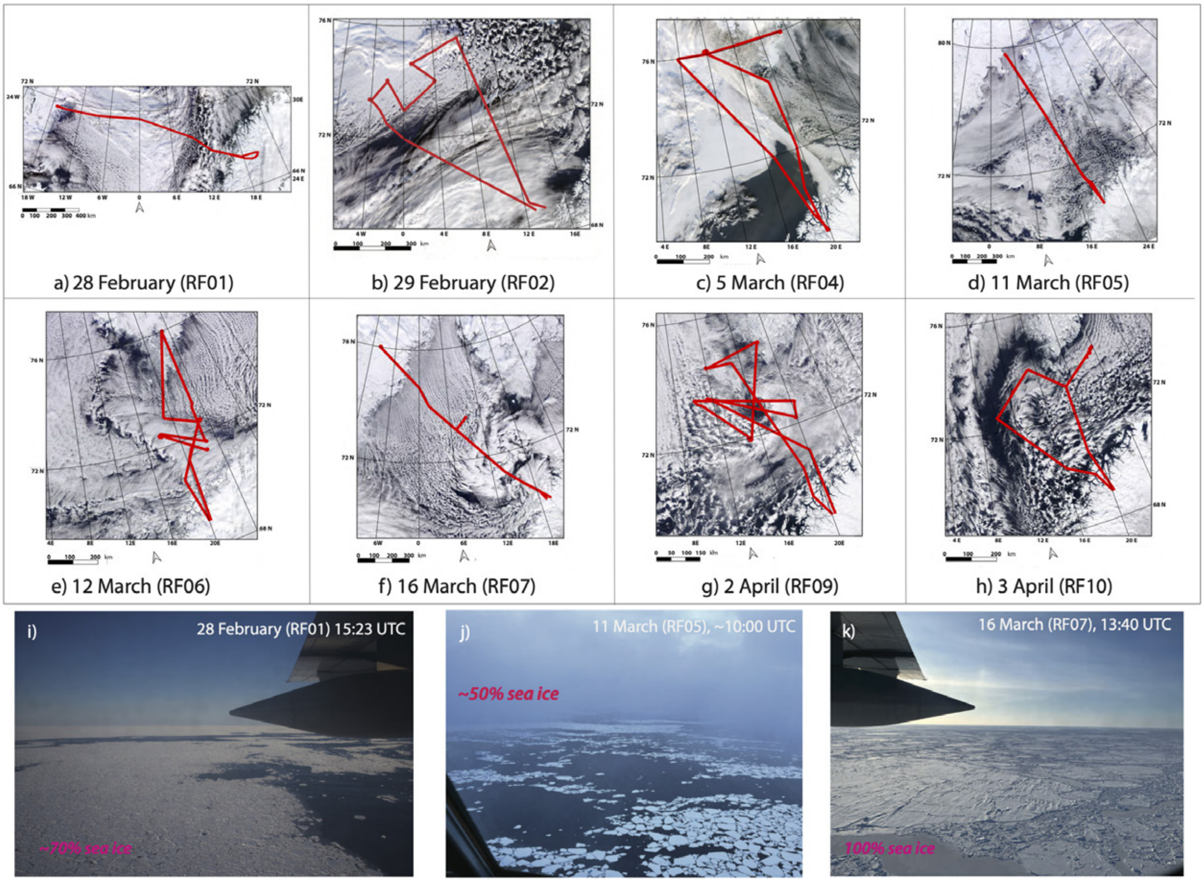

FIG. 3. MODerate resolution Imaging Spectroradiometer satellite imagery centered on the Research Flight (RF) tracks (in red) for a) 28 February (RF01; Terra), b) 29 February (RF02; Terra), c) 5 March (RF04; Aqua), d) 11 March (RF05; Terra), e) 12 March (RF06; Terra), f) 16 March (RF07; Terra), g) 2 April (RF09; Aqua) and h) 3 April (RF10; Aqua), all of 2024. Spatial domains vary. Arome-Arctic model output depicting lower atmospheric instability, sea level pressure and surface winds for each flight day shown in Fig. A4. Bottom row: Photos at flight endpoints for a) 28 February (~ 70% sea ice fraction, b) 11 March (~ 50% sea ice fraction and c) 16 March (fully ice-covered). photo credits: ER, GM, PZ respectively.

2. Campaign Hypotheses

CAESAR is designed to provide observations on marine CAO processes currently under-resolved in models (Field et al. 2017; Day et al. 2024). These observations are of turbulence, aerosol characteristics (both CCN and INP), the partitioning of cloud and precipitation between (supercooled) liquid and ice, and the spatial organization of the clouds and precipitation, all acquired within

Accepted for publication in *Bulletin of the American Meteorological Society.* DOI 10.1175/BAMS-D-25-0241.1.

the thermodynamic and dynamic context of the CAO lifecycle. CAESAR is loosely organized by the following five hypotheses encompassing the full fetch of CAO inception, evolution, and termination.

H1 air-sea exchange and the boundary layer. The boundary layer structure over the Arctic ice discernably influences subsequent cloudy boundary layer development.

H2 aerosols. The major ice-nucleating particle (INP) source is the free troposphere rather than the boundary layer, with immersion freezing of super-cooled liquid dominating the ice nucleation, while oceanic emissions are the primary cloud condensation nuclei (CCN) source.

H3 clouds and precipitation. Secondary ice production (SIP) increases with fetch while remaining insufficient to fully consume the liquid mass. SIP becomes more pronounced when clouds can produce cloud droplet diameters $\geq 20\ \mu$m. SIP is symptomatic of cloud morphological transitions to open cells.

H4 mesoscale organization. Cloud morphological transition timing is more correlated to precipitation than to wind shear, air-sea temperature differences, or lower-tropospheric instability.

H5 polar lows. Polar lows become initiated when destabilizing CAO-induced heat fluxes occur within a convergent frontogenetic shear zone, with intensification arising through interaction with an upper-level potential vorticity anomaly.

3. Campaign Overview

The NSF NCAR C-130 research plane can reach the Greenland MIZ from the deployment base of Kiruna, Sweden, a distance of over 1400 km, supporting the CAESAR goal of full-fetch CAO sampling. The campaign took place from 28 February 2024 through 3 April 2024, during which time the sea ice extent over the Greenland Sea increased to match that typical during the late 1990's (Fig. 1a). This is consistent with known inter-annual variability, wherein persistent synoptic atmospheric circulations (Fig. 2) support sea ice growth (Siew et al. 2023). Cold open water within thin oceanic mixed layers can quickly develop surface ice when exposed to cold air, and predominantly northerly winds will also mechanically push sea ice southward. In this scenario, the CAO-produced new ice counteracts Arctic surface warming, challenging trend attribution (Screen et al. 2025).

Accepted for publication in *Bulletin of the American Meteorological Society.* DOI 10.1175/BAMS-D-25-0241.1.

TABLE 2. Flight Summaries and Notes

Research Flight (RF) date (2024)	hours dropsondes	**Flight Synopsis** (spirals, S; ramps, R; below-cloud leg, BC; above-cloud leg, AC; porpoises, P)
RF01 28 February	5.85 15	**Greenland** marginal ice zone, 71°N, 17°W endpoint S-1; R-0; BC-2; AC-1; P-3
RF02 29 February	7.13 5	along+across CAO sampling, **closed-to-open** cell transition S-5; R-0; BC-3 along wind; AC-4 across wind; P-0; campaign-maximum CCN/N_d
RF04 5 March	6.62 3	warm air intrusion with dust forecasted (did not verify) S-2; R-0; BC-1 across wind; AC-2, 1 along wind; P-0
RF05 11 March	5.75 18	**Greenland** marginal ice zone, 79.6°N, 5°E endpoint S-0; R-3; BC-2; AC-2; P-6
RF06 12 March	6.37 9	**quasi-Lagrangian resampling**, south of Svalbard S-0; R-0; BC-1; AC-2; P-9
RF07 16 March	6.6 36	**Greenland** sea ice, 78°N, 10°W endpoint, polar low crossed enroute S-1; R-0; BC-4 (1 across wind); AC-5 (1 across wind); P-6
RF09 2 April	8.0 17	coastal **polar low**, modified rosette flight pattern with 5 transects S-1; R-1; BC-2; AC-3; P-12
RF10 3 April	7.55 13	**local CAO** sampling, 1 young and 1 mature S-1; R-0; BC-2; AC-5; **P-23**
Total Flights 8	53.87 hours 116 sondes	**3 full-fetch, 2 polar low, 1 Q-Lagrangian, 2 local CAO, 2 warm air intrusion** S-11; R-4; BC-17; AC-24; P-62

[1]Of 117 sondes released, 116 have complete thermodynamic information, and 112 include winds.

The NSF NCAR C-130 research plane deployed a large payload of in situ and remote sensors (Table A1). The campaign sampled a range of outbreaks at different stages of cloud development over the course of 8 research flights (Fig. 3, Table 2). Flights followed a typical pattern in which the plane first flew a high-altitude level leg to survey the cloud deck from above with remote sensors and dropsondes, then performed a slow spiral descent at the furthest point to comprehensively profile the aerosol, gas and water vapor isotope characteristics. This was done to establish the upwind conditions for the subsequent cloudy boundary layer development. Thereafter, the plane conducted a combination of legs of minimum-altitude level (150 m or higher), cloud profiling, and above-cloud legs. In total, 9.7 hours were devoted to collecting in situ cloud data, weighted towards the later flights, compared to 1.5 hours spent below the cloud.

Three flights best exemplify the CAESAR vision of reaching the Greenland's MIZ and retracing the boundary layer flow first interrogated with remote sensors, back to Norway. The MIZ endpoints had sea ice fractions of ~ 70% on 28 February and ~50% on 11 March (Fig. 3a, d; the 11 March flight was foreshortened by a North Atlantic Treaty Organization exercise). On 16 March, the flight reached cloud-free conditions over a sea ice fraction of 100% (Fig. 3f), launching 36 dropsondes en route. This 'golden case' comes closest to matching the CAESAR idealization. Three other

Accepted for publication in *Bulletin of the American Meteorological Society.* DOI 10.1175/BAMS-D-25-0241.1.

flights sampled CAOs arriving from the east off of the Barents Sea MIZ (5 March, 12 March, 3 April; Fig. 3c, e, h). The close proximity of the Barents MIZ allowed an express quasi-Lagrangian resampling of a previously-sampled air mass on the 12 March flight. The flight on 29 February was unusual for sampling a closed-to-open cell transition (Fig. 3b, Ephraim et al. 2026), as opposed to also involving cloud streets. Two flights were able to sample polar lows, despite an a-priori expectation a polar low might be too difficult to forecast to support a flight plan: the 2 April flight comprehensively sampled a polar low using a rosette pattern to fly above, below, and within the polar low (Fig. 3g, Newman et al. 2025), while the 16 March flight sampled a CAO that ultimately merged with another CAO to support a polar low. The last flight, on 3 April (Fig. 3g), was devoted to increasing statistics on cloud super-cooled liquid and ice vertical structure. Warm air intrusions were not a focus of the CAESAR campaign, but were neverthless partially sampled on 29 February (in which warm, moist free-tropospheric air overlaid a CAO) and 5 March, for which a dust forecast did not verify. Throughout, the aircraft remained west of 24 °E to maintain distance from Russian airspace. Overall, on 6 flights, upwind conditions of CAOs were sampled over either the Greenland or Barents MIZs, addresssing hypothesis $H1$. INP and CCN data were collected both above and within the boundary layer on all the flights (hypothesis $H2$), ice and liquid microphysics were characterized using both in situ and remote sensors on all flights (hypothesis $H3$). The cloud mesoscale organization was characterized using the remote sensors and satellite data (hypothesis $H4$) on all flights, and polar lows were expressly characterized in 2 flights.

Aircraft troubles led to fewer research flights than initially planned, but the large suite of well-performing instruments captured complementary measurements able to provide insight into the CAESAR hypotheses. Detail on the individual measurements and an instrument table is provided in the Appendix, with examples of the information gleaned provided below, along with references to the most relevant hypothesis abbreviated as $H1$, $H2$, $H3$, $H4$ and $H5$.

4. Gas Measurements Indicate Varied Air Mass Origins

At process scales, the carbon monoxide (CO), ozone (O_3) and nitrous oxide (N_2O) concentrations can determine entrainment velocities relevant to determining CCN and INP origins ($H2$), even after entrainment and mixing ($H1$) (Ephraim et al. 2026). CO and N_2O primarily originate from anthropogenic emissions in the early spring (Platt et al. 2022). In the mean, spring CO

Accepted for publication in *Bulletin of the American Meteorological Society*. DOI 10.1175/BAMS-D-25-0241.1.

decreases with height, whereas O_3 increases with height (Jonas et al. 2026). A record of over 30 years of surface-based gas measurements and ozonesondes at Zeppelin Observatory on Svalbard indicates annual Arctic total column ozone has recovered, dominated by springtime values, while tropospheric ozone has declined in response to air quality regulation, more clearly observed in the spring (Platt et al. 2022; Jonas et al. 2026). In situ free-tropospheric gas measurements in the Arctic remain scarce, however, lending value to the CAESAR aircraft measurements.

The close anti-correlation of high-O_3 with low-CO air within CAESAR air samples indicate stratospheric air intrusions at the surface (Fig. 4), mostly gathered further north (not shown). The highlighted population is only 1% of the total gas samples, but the same CO:O_3 ratio can be distinguished within other low-altitude gas mixtures. Some low-altitude samples are enriched in CO (> 130 ppbv) but depleted in O_3 (≤ 50 ppbv). This is characteristic of episodic bromine and iodine chemistry occurring at both sea ice and ocean surfaces (Herrmann et al. 2019; Benavent et al. 2022). Higher-altitude air containing positively-correlated CO and O_3 is also enriched in N_2O (not shown) is consistent with advection of anthropogenic air into the Arctic from south of the polar dome along a constant isentrope line. During individual flights, the gas concentrations provide information on air mass origins, relevant to $H4$ but also $H1$. Mean values of O_3 and CO are consistent with March-mean O_3 concentrations at Villum Research Station and Zeppelin of between 32-40 ppbv, and March-mean CO concentrations at Zeppelin of approximately 150 ppbv (Platt et al. 2022; Whaley et al. 2023).

5. Small Aerosols Dominate the Free Troposphere while Large Aerosols Dominate the Boundary Layer

Total aerosol number (N_{total}) concentrations range from 50 to 700 cm^{-3} (Fig. 5a), based on a particle number distribution merged from five aerosol sensors spanning diameters from 10 nm to 0.5 mm (Cai et al. 2026). Comparisons between free troposphere (FT; > 1 km) and boundary layer (BL; < 500 m) measurements both confirm and refute $H2$ (the arbitrary altitude designations effectively select for the near-surface and above-cloud level flight legs). FT N_{total} exceed BL N_{total}, although median FT and BL CCN and accumulation-mode aerosol concentrations are similar at 90-110 cm^{-3} (Fig. 5b, c). The ocean is one likely source for the larger accumulation-mode aerosol, given a sea spray aerosol flux that increases with wind speed U as approximately $U^{3.41}$ (Clarke

Accepted for publication in *Bulletin of the American Meteorological Society.* DOI 10.1175/BAMS-D-25-0241.1.

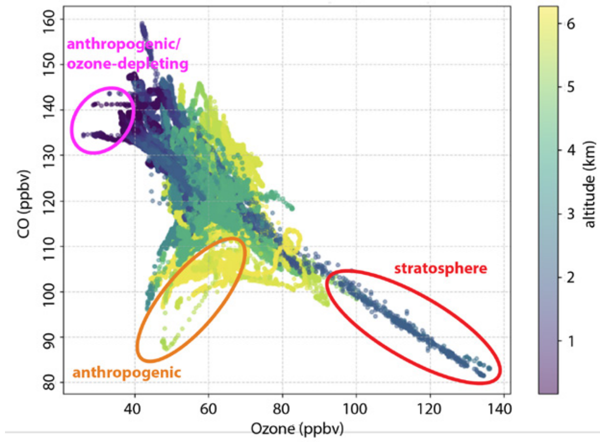

FIG. 4. Carbon monoxide (CO) versus ozone (O_3) concentrations (ppbv), restricted to north of 82°N, colored by altitude, from all flights. Air defined by CO $\leq$ 100 and $O_3 \geq$ 90 ppbv sampled at altitudes < 2 km is characteristic of stratospheric origin. High-altitude CO between 90-110 ppbv positively correlated with O_3 is indicative of anthropogenic origin. High/low CO/O_3 concentrations at low altitudes can indicate anthropogenic air for which O_3 is depleted through halogen chemistry over both water and sea ice.

et al. 2006), consistent with a BL aerosol mode diameter and volume concentrations that exceed FT values (Fig. 5d-e). This partially confirms *H*2. CCN can also originate from Aitken mode aerosol activated within strong updrafts, as deduced for the southern oceans (McCoy et al. 2021), although analysis for one flight suggests entrainment from the FT primarily dilutes BL CCN (Ephraim et al. 2026). Median refractory black carbon mass concentrations (M_{rBC}) are slightly higher in the BL than the FT (12 and 6 ng m^{-3} respectively, Fig. 5f), consistent with low-level transport within the polar dome (Schulz et al. 2019), but the highest M_{rBC} occurs in the FT, described more fully in Cai et al. (2026). Entrainment at cloud top can also bring in black carbon into the BL.

6. INP concentrations Likely Similar Between the Free Troposphere and the Boundary Layer

INP concentrations, drawn from three independent INP measurements evaluating immersion freezing (see Appendix), collectively span environmental temperatures from -30 °C to almost -5 °C (Fig. 5g). The concentrations based on the offline ice spectrometer are similar between the boundary layer and free troposphere, refuting *H*2, although individual flights are more varied (e.g., during RF02, INP concentrations were higher in the BL than above the CAO clouds; Ephraim et al. 2026). The online CFDC INP measurements that are closely colocated are also similar between

Accepted for publication in *Bulletin of the American Meteorological Society.* DOI 10.1175/BAMS-D-25-0241.1.

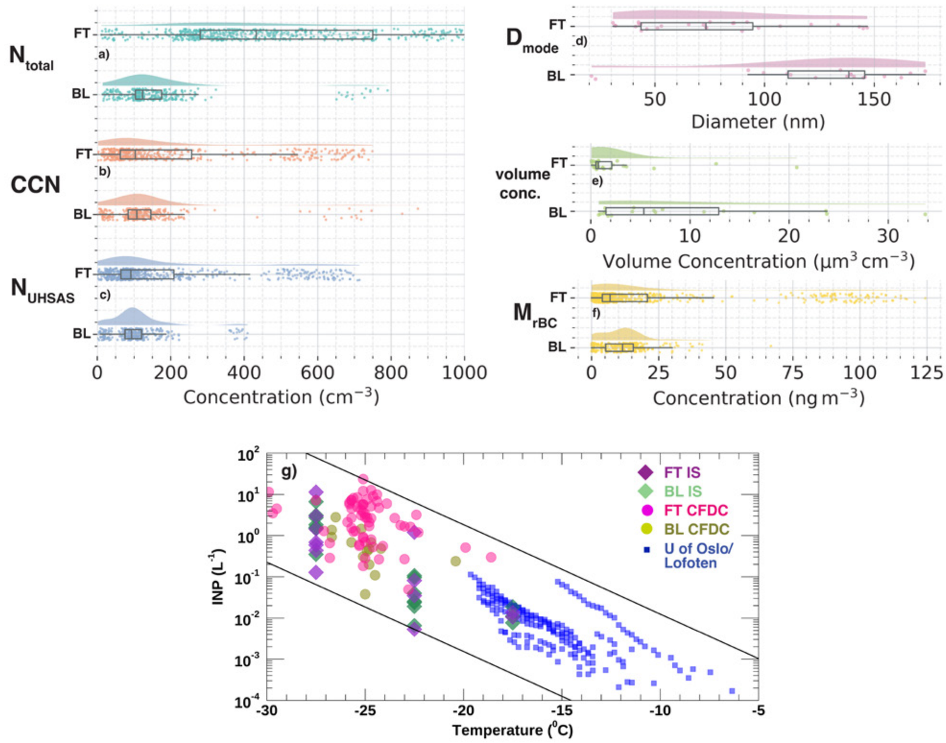

FIG. 5. Distribution within the free troposphere (FT) and marine boundary layer (BL) outside of cloud from all flights of a) total aerosol number concentrations (N_{total} in cm^{-3}), b) cloud condensation nuclei (CCN) concentrations (cm^{-3}) at 0.4% supersaturation from the Wyoming sensor for RF01-RF02 and the DMT sensor for RF04-RF10, c) Ultra-High Sensitivity Aerosol Spectrometer (UHSAS) accumulation mode aerosol concentrations (N_{UHSAS}, spanning 0.06-1 μm, in cm^{-3}). d) total aerosol mode diameter (D_{mode}, nm), e) total aerosol volume concentrations (μm^3 cm^{-3}) and f) Single Particle Soot Photometer (SP2) refractory black carbon mass concentrations (M_{rBC}; ng m^{-3}). a), d) and e) based on merged aerosol distributions (Cai et al. 2026). a)-f) depict median, 10th and 90th percentile, and 25th and 75th quartile values and 1 Hz data (Wyoming CCN measurements at 0.03 Hz). FT and BL samples from altitudes > 1 km and < 500 m respectively. g) CSU Continuous Flow Diffusion Chamber (CFDC) ice-nucleating particle (INP) concentrations > 1 km (pink filled circle) and < 500 m (olive filled circle) at instrument temperature. CSU Ice Spectrometer (IS) INP concentrations at ambient temperature > 1 km (purple diamonds) and < 500 m (green diamonds), with no destructive treatments applied. U of Oslo INP measurements near the town of Napp on the Lofoten peninsula, Norway, at ambient temperature from 3 CAOs (blue squares). Black lines encompassing the INP measurements correspond to $INP_{upper} = 10^{-0.2169T-4.0733}$ and $INP_{lower} = 10^{-0.2169T-7.1537}$. Aerosol concentrations at 1013 hPa and 298.15 K, and INP measurements at 1000 hPa and 273.15 K. All INP measurements based on immersion freezing. Airborne data are from all flights and exclude measurements made on the CVI inlet.

Accepted for publication in *Bulletin of the American Meteorological Society.* DOI 10.1175/BAMS-D-25-0241.1.

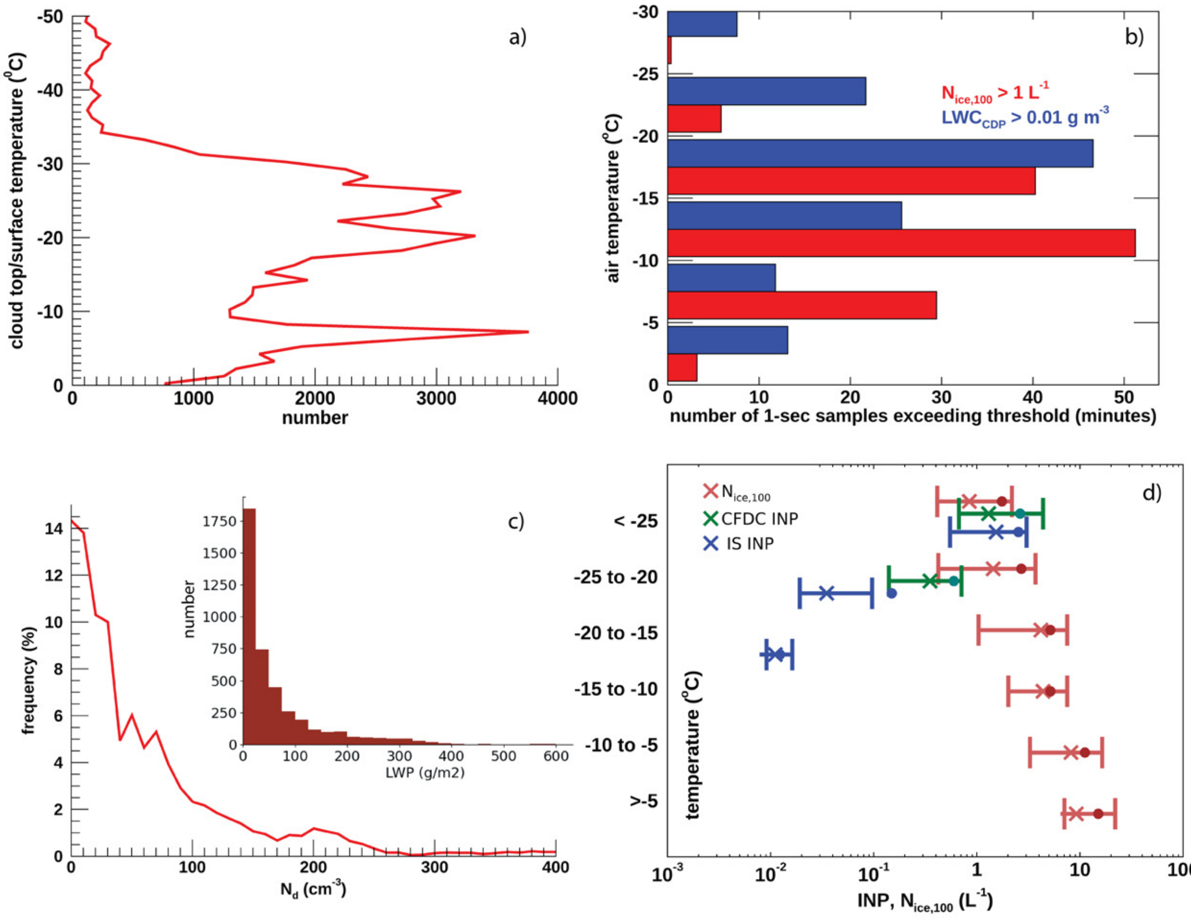

FIG. 6. a) Temperature distribution below the plane from the KT19 infrared radiometer, for all flights. b) Liquid and ice particle sampling time as a function of air temperature, in 5-degree temperature bins at ambient concentrations. Cloud is identified by inboard Cloud Droplet Probe (CDP_{in}) liquid water contents > 0.01 g m^{-3} (blue), Fast Two Dimensional Stereo (F2D-S) probe ice particle number concentrations for particle sizes > 100 μm (red; $N_{i,100}$) > 1 L^{-1}. c) CDP_{in} cloud droplet number concentration (N_d) frequency distribution with microwave-derived cloud liquid water path (LWPs; Ephraim et al. 2025) frequency distribution in upper right inset. d) INP concentrations (L^{-1}; green at the CFDC instrument temperature, sample period is significant at 90%; blue for the IS filter measurements at freezing temperature) and F2D-S (horizontal arm) $N_{i,100}$ (L^{-1} in dark red) at the in situ temperature, based on $N_{i,100}$ > 1 L^{-1} 1Hz samples only. INP and $N_{i,100}$ concentrations reported at 273.15 K and 1000 hPa. Median (crosses), 25th and 75th quartile ranges (lines), and mean values (filled circles) are indicated. Statistics are based on 22 and 29 CFDC INP samples within the -25 °C to -20 °C and < -25 °C instrument temperature ranges, respectively. Sampling constrained to north of 70°N for all figures, to > 3 km for panel a), and < 4 km for $N_{i,100}$, and ≤ 3 km for INP. CFDC INP data is lacking for 2 March (RF06), datasets otherwise encompass all flights. Ice particles are identified by sphericity thresholds < 0.7 (Korolev and Isaac 2003).

Accepted for publication in *Bulletin of the American Meteorological Society*. DOI 10.1175/BAMS-D-25-0241.1.

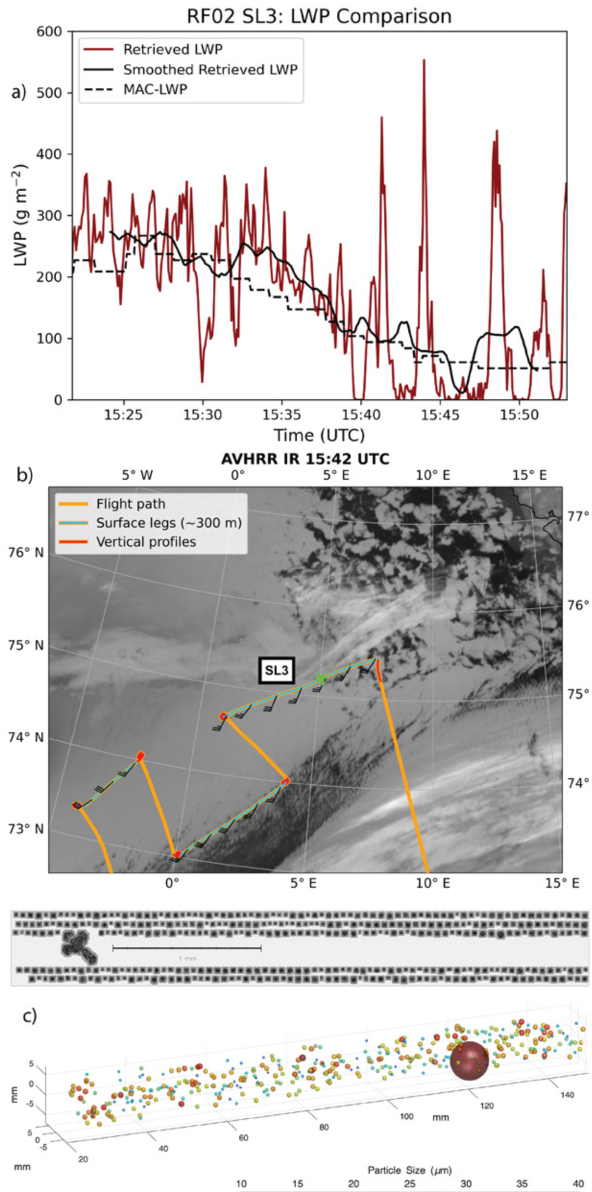

Fig. 7. New observations include a) GVR-retrieved LWP time series at native ~ 500 m resolution (maroon) smoothed (black solid) to match the satellite-derived 0.25 °-resolution Multisensor Advanced Climatology LWPs (MAC-LWPs; Elsaesser et al. 2017) (black dashed) across a closed-to-open cell transition on 29 January 2024 (RF02) 15:22-15:52 UTC, b) depicted on Advanced Very High Resolution Radiometer infrared imagery at 15:42 UTC as 'SL3'. Smoothed satellite-derived LWP values approximately match airborne-derived LWPs though miss LWP spikes in the cumulus regime. Precipitating snow may also differentially impact the retrievals. c) Top panel: reconstructed HOLODEC-II images, in no particular order, for 12 March RF06 10:26:26 UTC. Bottom panel: the 3-D positions for the same cloud particles. Ice particle in top panel shown as its sphere-equivalent in red. Particle sizes are exaggerated by a factor of 20.

Accepted for publication in *Bulletin of the American Meteorological Society*. DOI 10.1175/BAMS-D-25-0241.1.

the FT and BL, suggesting the appearance of higher FT CFDC values in Fig. 5g is primarily from sampling differences. The two lines encompassing the INP measurements can guide modeling representations. INP samples collected from 3 CAOs landfalling on the Lofoten peninsula, Norway during the CAESAR time period but not sampled by the plane extend measurements to warmer temperatures. INPs likely differ between the sea ice edge and Scandinavian coast, with the ocean potentially sourcing new INPs while cloud scavenging may be potentially reducing INP concentrations (DeMott et al. 2025). Overall, INP concentrations measured during CAESAR are similar to those measured during MOSAiC (Creamean et al. 2022) and COMBLE (Geerts et al. 2022), and less than those measured during ACAO (Raif et al. 2024).

7. Clouds with Tops ≤ -20 °C Support Liquid Water Paths up to 200 g m^{-2} and Secondary Ice Production

Cloud top temperatures (T_{ct}) are mostly between -30 °C to -20 °C (Fig. 6a; T_{ct} > -10 °C are from the warm air intrusion sampled on 5 March during RF04). Sea surface temperatures were typically ~ 3 °C, but intervening cloud and precipitation reduce infrared-derived measurements to < 0° C for 3% of the samples. Most particles are liquid at temperatures < -25 °C, transforming to mostly ice at > -15 °C (Fig. 6b). In situ profiles indicate more liquid at colder temperatures, increasing with height - even more convincing given that icing concerns encourage undersampling of super-cooled liquid. Cloud top temperatures do not reach the homogeneous freezing threshold of ~ -38°C. The increase in ice at warmer temperatures indicates an efficient liquid-to-ice conversion, with the longer near-surface level legs primarily sampling ice precipitation (not shown).

The Cloud Droplet Probe measured (liquid) cloud droplet number concentrations (N_d) mostly below 100 cm^{-3} (Fig. 6c), similar to the median sub-cloud CCN and accumulation-mode aerosol concentrations (Fig. 5b, c). N_d did reach 400 cm^{-3} during the 29 February RF02 flight (Fig. 6c, Fig. A1), for which below-cloud CCN concentrations exceed 700 cm^{-3} at 0.4% supersaturation (Fig. 5b), the highest in the campaign. The high aerosol loading, accompanied by slightly elevated M_{rBC}, can be traced back to emissions from Norilsk, Siberia (Ephraim et al. 2026), a town built around a nickel and heavy metal processing plant (Bauduin et al. 2014). Northern Asis also contributed significantly to the springtime rBC and accumulation-mode aerosol measured further

Accepted for publication in *Bulletin of the American Meteorological Society.* DOI 10.1175/BAMS-D-25-0241.1.

north during the Multidisciplinary drifting Observatory for the Study of Arctic Climate (MOSAiC; Boyer et al. 2023).

Remotely-retrieved cloud liquid water paths (LWPs), averaged over ~ 500 m spatial scales, mostly remain below 200 g m^{-2} (Fig. 6c, inset), akin to Abel et al. (2017) and to values for sub-tropical stratocumulus clouds (Zuidema et al. 2012). These retrievals originate from an upward-looking 183-GHz G-band Vapor Radiometer able to resolve mesoscale (~ 600 m) variations of the super-cooled LWP (Ephraim et al. 2025). These add granularity and help assess corresponding microwave satellite-derived values (Fig.7a-b; Elsaesser et al. 2017) in this challenging regime. The two retrievals confirm each other in the closed-cell regime, while the higher-resolution airborne values better capture the strong LWP spikes associated with open-celled cumulus clouds and their updrafts (not shown). Measurements of super-cooled liquid, vertically-resolved and vertically-integrated, are critical for addressing $H3$ and $H4$. Measurements have typically relied on satelite-derived values (e.g., Juliano et al. 2026).

The ice particle number concentrations are primarily measured by the Fast Two Dimensional Stereo (F2D-S). Median $N_{i,100}$ are < 10 L^{-1} irrespective of in situ cloud temperature (Fig. 6d). At < -25 °C, median INP values of 1-2 L^{-1} match $N_{i,100}$ well, indicating primary ice nucleation is likely dominating at the colder temperatures higher in the cloud, consistent with Carlsen and David (2022), Pasquier et al. (2022), Raif et al. (2024), Jimenez et al. (2025) and DeMott et al. (2025). Ice generated near cloud top will also populate the cloud at lower altitudes. At warmer cloud temperatures, median $N_{i,100}$ exceed INP concentrations measured near cloud top, but only slightly.

The relative contribution of secondary ice production (SIP, or multiplication by ice particles already present), to $N_{i,100}$ values lower down in the cloud still needs to be systematically determined. Temperatures remain colder than the -3 °C to -8 °C range of the rime-splintering regime focused on by other campaigns (e.g., Abel et al. 2017; Schäfer et al. 2024; Biggart et al. 2026; Pearson et al. 2026). Droplets with diameters > 100 μm are occasionally observed, and can potentially freeze and fragment (Korolev and Leisner 2020). Ice breakup, including through collisions with rimed particles (Grzegorczyk et al. 2023), is encouraged by cloud temperatures in the dendritic growth zone (-12 °C to -18 °C; Fig. 6b). These processes can be explored further using measurements from the Holographic Detector for Clouds v.2 (HOLODEC-II) probe, measuring particles > 12 μm

Accepted for publication in *Bulletin of the American Meteorological Society.* DOI 10.1175/BAMS-D-25-0241.1.

in diameter (Fig. 7c). The HOLODEC-II captures a size range (40 μm-100 μm) not well resolved by conventional probes. Importantly, and unlike conventional probes, the HOLODEC-II captures the true spatial distribution of ice and liquid particles ($H3$) within a volume of 15 cm^2. The RF02 HOLODEC-II data does not show any drizzle freezing-fragmentation events (Ephraim et al. 2026), but this is just one flight. The phase discrimination information provided by the HOLODEC-II and the Nevzorov probe is also critical for parameterizing phase inhomogeneity within models (Korolev and Millbrandt 2022).

8. The 16 March 2024 cold air outbreak (RF07): A golden yet unique case?

The 16 March flight came closest to achieving a CAESAR campaign goal: tracking a CAO from clear-sky conditions over a fully ice-covered surface, through its evolution into ever-larger cloud streets converging, in this case, into a polar low (Fig. 3f). High pressure over Greenland paired with low pressure to the east established optimal synoptic conditions for strong southward winds down the Fram Strait. As the plane flew northwest towards Greenland at an altitude of 5 km, dropsondes, released every ~5 minutes, documented the thermodynamic profiles below the plane (Fig. 8). At the plane's final reach (80 °N, 10 °W), the surface boundary layer was only ~ 60 m deep, too shallow for the plane to investigate in situ.

Notable in the dropsondes is the transition of the cold stable layer over the sea ice to a deeper surface-based layer warmed by surface fluxes closer to the Norwegian coast. The spiral descent (data not shown) reveal a layering of aerosol and ozone, with a well-mixed layer between altitudes of 500-1000 m. O_3 and CN decrease between 3.5-4 km altitude and the surface (from 50 to 40 ppbv for O_3, 200 to 150 cm^{-3} for CN), while accumulation-mode aerosols (UHSAS) and CCN increase from approximately 30 to 60 cm^{-3} and 10 to $\gtrsim$50 cm^{-3}, respectively, highly variable in altitude. The changes with altitude are consistent with Fig. 5.

ERA5 backtrajectories initialized at 500 m (not shown) indicate north-northeasterly flow over leads within the sea ice (apparent in satellite imagery), and this advection may explain the increase in near-surface aerosol. Sea ice surface temperatures are initially near -30 °C (Fig. 9a), with dropsondes indicating near-surface air temperature of -25 °C (Fig. 8). The subsequent 30-minute minimum-altitude leg back to open water further reveals advective influences from the northeast, with both temperatures gradually warming en route. Infrared-derived surface temperatures indicate

Accepted for publication in *Bulletin of the American Meteorological Society.* DOI 10.1175/BAMS-D-25-0241.1.

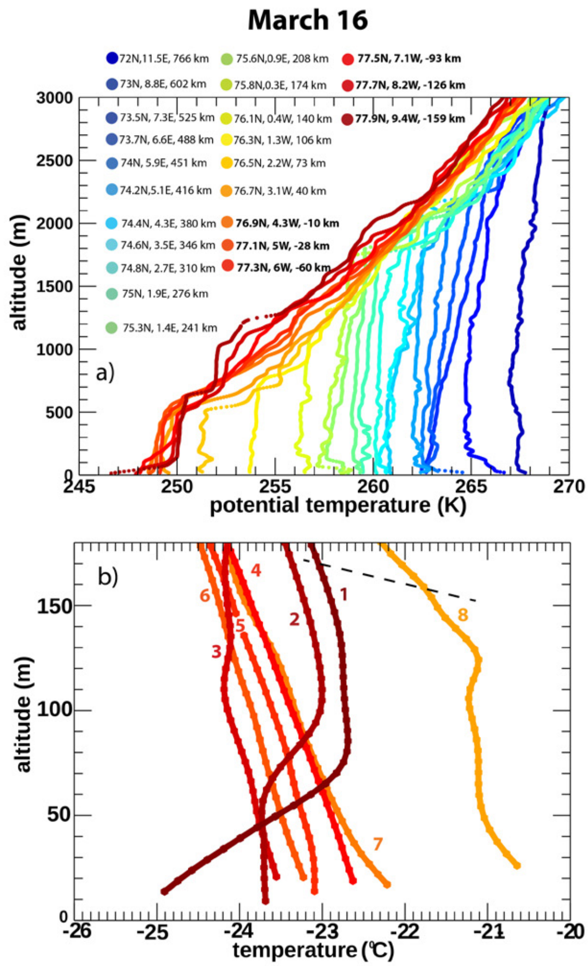

Fig. 8. a) Dropsonde-derived potential temperature profiles (0 to 3 km in altitude) along the March 16 cold-air outbreak, spaced ~ 5 degrees (~ 5 minutes in time) apart. Inset indicates location and distance to the sea ice edge in km. The sea ice edge is at 77 °N and 4°W. b) the 8 temperature profiles at the furthest end of the flight, spanning 0 to 170 m in altitude. The thin dashed black line indicates the aircraft altitude decreased from 170 m, at the beginning of the return mininum altitude leg, to 150 m, after ~230 km in flight.

when open water comes into the radiometer's view, with surface temperatures remaining < 0° C most likely still indicating a contribution from floating ice. At flight level, CO gradually increases from 140 to 142 ppbv and O_3 decreases more substantially from 39 to 34 ppbv (Fig. 8b), suggesting originally anthropogenic air that has lost O_3 to the surface during transit (see Fig. 4 for context).

The water vapor mixing ratio also increases, as does a water vapor isotope measure that is particularly reflective of surface evaporation (δD). δD measures the difference in the excesses in

Accepted for publication in *Bulletin of the American Meteorological Society*. DOI 10.1175/BAMS-D-25-0241.1.

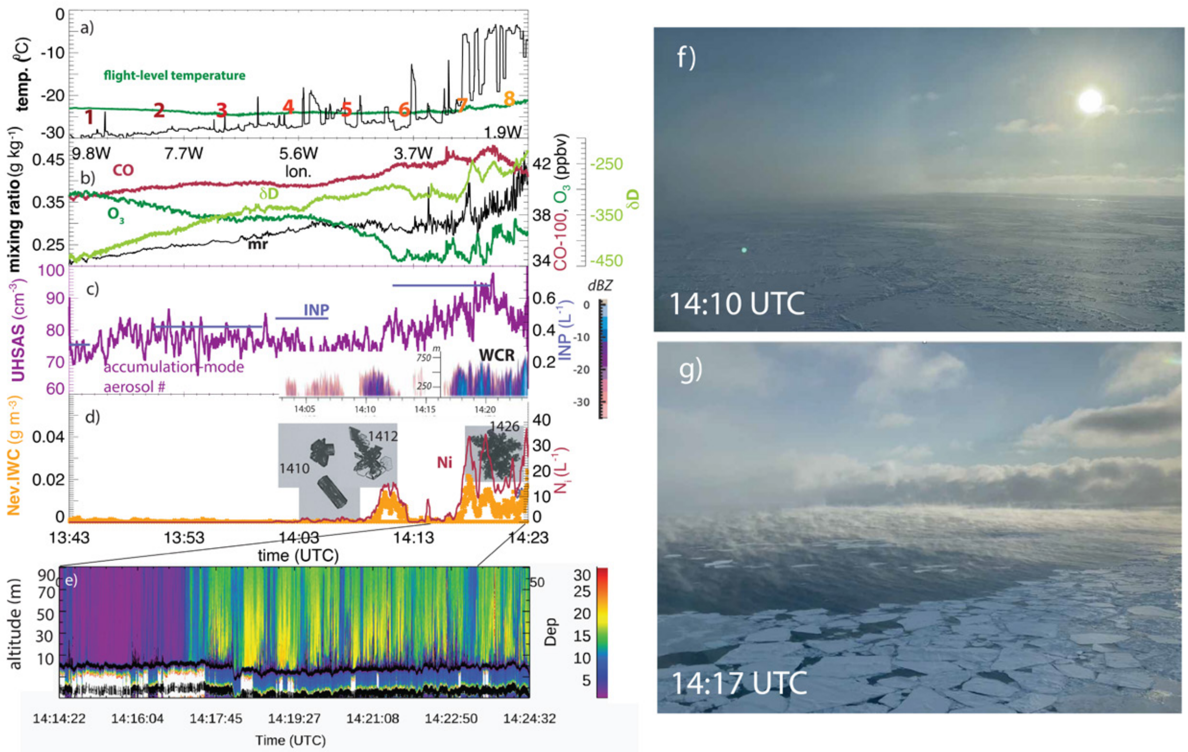

Fig. 9. 16 March 2024 RF07 surface leg, from 13:43 UTC after the plane finished its spiral descent to reach ~ 170 m, crossing the MIZ to be at ~ 150 m altitude by 14:23 UTC. a) the infrared-inferred surface temperature and flight-level temperature (green), with locations corresponding to dropsonde temperature profiles (Fig. 8) matched by color and number. b) trace gas measurements (CO-red, O_3-dark green, δD-lime green,described in main text, mr-black, water vapor mixing ratio). c) UHSAS CCN (purple) and CFDC INP (dusky blue). inset shows upward-looking WCR reflectivity. INP values at instrument temperatures near -25°C, cooler than in situ flight level tempreatures of -21 to -23 °C. d) F2D-S N_i (red, no size threshold) and Nevzorov IWC (dark yellow; calculated from total-liquid water content) with select PHIPS images. The plane entered the surface-based thermodynamic layer at 14:03 UTC. e) downward-looking MARLi depolarization ratio. The black line indicates the surface, with sea ice in white and open water in dark blue below the black line. f) photo at 14:10 UTC includes a faint ice halo around the sun g) steam fog over open water at 14:17 UTC. photo credits: PZ.

two distinct measured water isotopologues ($HD^{16}O$, where D is a deuterium replacing the protium in hydrogen, and $H_2^{18}O$) relative to standard water reference values as: $\delta D = \delta HD^{16}O - 8 \times \delta H_2^{18}O$ (Dansgaard 1964). The moisture recharge by surface evaporation is enriching the atmosphere in δD, explored on a larger scale within Aemisegger and Sjolte (2018) . The δD value also becomes

Accepted for publication in *Bulletin of the American Meteorological Society.* DOI 10.1175/BAMS-D-25-0241.1.

more variable once more open water is reached. Future analysis will apply the isotopes ($H_2^{16}O$ is also measured) to discriminate ocean evaporation influences from precipitation-induced changes ($H2$). Precipitation preferentially depletes heavy isotopes from the atmosphere, decreasing $\delta HD^{16}O$, while hydrometeor sublimation and evaporation further exchange isotopes with the surrounding below-cloud environment (Sarkar et al. 2023; Wahl et al. 2024). Fast-response (25 Hz) water vapor mixing ratio hygrometer, temperature and vertical wind measurements support the derivation of flight-level latent and sensible heat fluxes reaching 170 and 250 W m^{-2}, mostly at scales < 2.5 km (McGinnity et al. 2026), relevant to $H1$ and $H4$.

Acccumulation-mode aerosol number concentration and INP concentrations remain steady at ~ 75 cm^{-3} and 0.5 L^{-1} respectively, until open water is reached (Fig. 9c). The surface-based layer deepens enough to reach the plane by 14:03 UTC. Cloud particles are first detected in situ at 14:06 UTC. The Nevzorov cloud probe indicates no liquid is present, with the Particle Habit Imaging and Polar Scattering (PHIPS) probe resolving condensationally-grown columns, side planes and other polycrystals (a halo is present around the sun from ice crystals in Fig. 9f). N_i concentrations of 10-40 L^{-1} (Fig. 9d, based on all F2DS measurements) even indicate secondary ice production is already occurring.

The question arises: How were the ice particles nucleated? Surface wind speeds are initially < 4 m s^{-1}, below the 7-9.5 m s^{-1} threshold at 10 m altitude for blowing snow (Gong et al. 2023). The wind speeds increase to ~ 9 m s^{-1} by the first water opening, but filter analysis indicates a mineral INP. Prior work concludes sea ice is, paradoxically, a poor source of INPs (Carlsen and David 2022; Creamean et al. 2022; Boyer et al. 2023). More remarkable is the coincidence of the ice particles with the strong moisture plumes emanating off of the surface (Fig. 9e). These are detected by the first deployment of the Multi-function Airborne Raman Lidar (MARLi) upon the C-130 plane, providing sub-plane vertically-resolved temperature and water vapor profiles as well as of aerosol and cloud backscatter colocated with sea-ice and open ocean surfaces. MARLi depolarization ratios are near zero within the lowest 10 m (Fig. 9e), consistent with water vapor condensing into liquid ("sea smoke") at (dropsonde-derived) air temperatures between -22 °C to -25 °C. The depolarization ratios increase at altitudes ≥ 20 m, indicating ice. The strong thermal updrafts would increase opportunities for ice nucleation (e.g., Raatikainen et al. 2022) by dust at the air temperatures of -25 °C (Murray et al. 2012). Turbulent mixing with colder environmental air

Accepted for publication in *Bulletin of the American Meteorological Society*. DOI 10.1175/BAMS-D-25-0241.1.

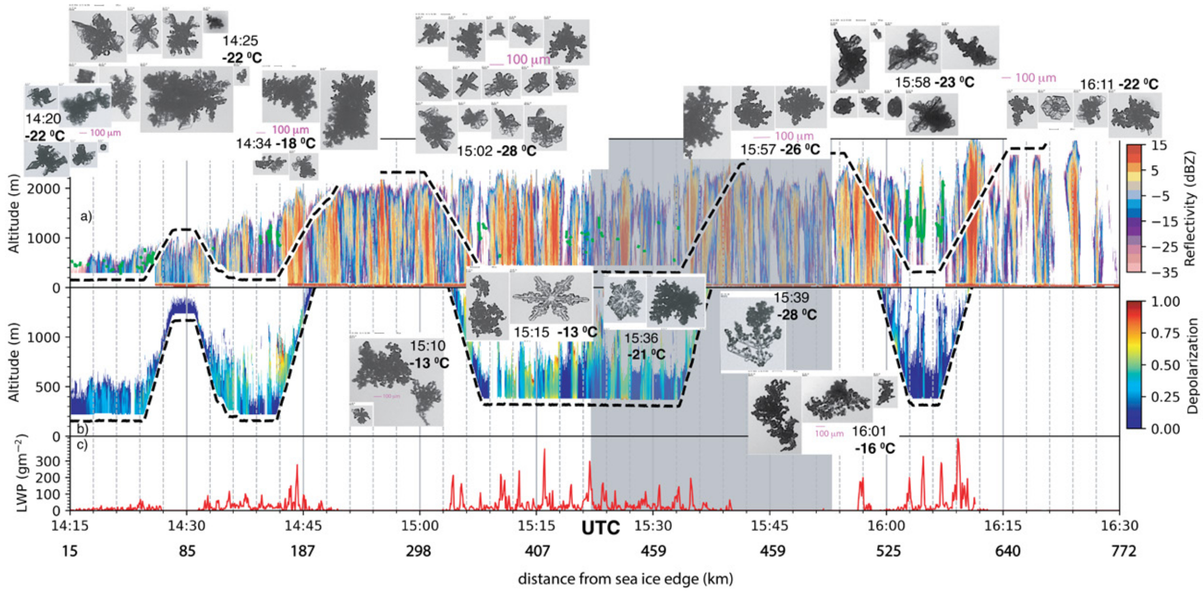

FIG. 10. 16 March RF07 14:15 UTC-16:30 UTC (overlapping for 8 minutes with timeseries shown in Fig. 9) transect back from Greenland to Norway. a) WCR radar reflectivity with PHIPS particle imagery superimposed and the WCL-determined cloud base height where available (green filled circles), b) WCL depolarization indicating the presence of ice versus liquid (high versus low depolarization), c) GVR-determined LWP. The planview flight track is indicated in Fig. 2. The greyed portion from 15:22 UTC - 15:33 UTC corresponds to the C-130 transect perpendicular to the main transect.

will generate high supersaturations in these thermal plumes, with the water vapor isotope analyzer indicating RH values exceeding water saturation at flight level. These also favor a quick vapor depositional growth process. By 14:17 UTC, the plane is over open water, indicated by MARLi (Fig. 9e, dark blue color below the surface), and ice production increases. In summary, these observations remain consistent with $H4$.

The improved ice particle habit identification from the PHIPS probe indicates ice habits are initially polycrystals (snowflakes from multiple ice crystals; Fig. 10) during the return flight over open water to the Scandinavian coast. Flight-level temperatures rise to -15 °C and N_i concentrations decrease to ~ 10 L^{-1} by the 14:36-14:42 UTC surface leg (Fig. A2). The ice water content (IWC) simultaneously increases slightly with distance from the sea ice edge, consistent with an increase in aggregation detected by a habit classification applied to the PHIPS data (Fig. S3). Aggregation is also commonly-observed at Svalbard (Chellini et al. 2022). The third surface leg, from 15:02-15:27

Accepted for publication in *Bulletin of the American Meteorological Society*. DOI 10.1175/BAMS-D-25-0241.1.

UTC, samples fully-formed snowflakes and rimed particles at temperatures between -14 °C to -12 °C, with IWC often > 0.2 g m^{-3}. Clouds are more broken and LWP is more variable, exceeding 200 g m^{-2} in places. This is consistent with updraft-driven cumuliform clouds (behavior documented more fully for RF02 in Ephraim et al. 2026). Individual images suggest riming becomes more common as the clouds deepen, for example during the 15:35-15:40 UTC ascent, for which profiles of LWC, N_d, IWC, and N_i indicate multiple layers of liquid and ice (not shown). Although the radar imagery indicates a more open cellular structure after 16:00 UTC, the visible cloud fraction does not obviously decrease (Fig. 3f), consistent with some satellite-based analyses (McCoy et al. 2017).

9. Polar Lows combine strong surface fluxes with upper-level vorticity anomalies

Polar lows are powerful and difficult to forecast. Serendipitously, not one, but two, polar lows were sampled. Both formed in CAO environments, with cores of relatively warm air. The flight on 2 April (RF09; Fig. 3g), documented fully in Newman et al. (2025), included 5 aircraft traverses across the low, of which one is shown in Fig. 11a-b. This low formed under northerly flow in the lee of Svalbard and involved the merger of a mature long-fetch CAO from the Fram Strait with a short-fetch, shallower, and colder CAO that emerged from the Barents MIZ. This merger occurred along a frontogenetic convergent shear zone. As the northerly flow wrapped around the developing low, the wind speeds and surface heat fluxes decreased. The air on the east side also was cooler due to large-scale zonal baroclinicity consistent with the northerly flow aloft. Decoupled CAO convection ascending over this cooler air evolved into a stratiform cloud deck (far right of Fig. 11b). Aside from this cloud deck, cloud tops around this polar low were around 2.5 km, similar to the open-cellular convection west of the low. Interestingly, this flight also sampled the highest INP concentrations of the campaign, mixed in with relatively fresh anthropogenic pollution (Cai et al. 2026).

The other polar low on 16 March 2024 (RF07), not yet documented elsewhere, occurred in the presence of larger surface heat fluxes and lower-level instabilities. The more convective polar low, immersed in an intense CAO, reached altitudes of 5 km (Fig. 11c-d), underneath a very cold, low tropopause. Convection reaching 2.5 km advected from the northwest, then transitioned across a convergence line into larger convective cloud complexes (Fig. 11d), with some anvil formation

Accepted for publication in *Bulletin of the American Meteorological Society.* DOI 10.1175/BAMS-D-25-0241.1.

and up- and down-drafts reaching up to ~ 5 m s^{-1} (not shown). The upper-level positive potential vorticity formation present in both cases is consistent with $H5$ and likely results from interaction of the upstream large-scale flow with the orography of Svalsbard.

10. Outreach increases Impacts

Value-Added Products (VAPs) ease use of the CAESAR datasets by the larger research community. The merged total aerosol size distribution dataset (Cai et al. 2026) is one example of a value-added product (VAP) meta-dataset. Also available are movies compiled of camera imagery and selected data (Table A2). Cloud microphysical and remote sensor VAPs are available and will continue to receive additions over time. The suite of remote sensors provides opportunities for imaginative, combined retrievals that are now facilitated by merging available retrievals into one common time and vertical spacing grid. The VAP currently includes the WCL-derived cloud base and WCR-derived cloud top heights. Further additional available datasets contain satellite products and model output (Table A3).

Field campaigns bring in a generation of new scientists and draw attention to significant phenomena. CAESAR built on these benefits by including multiple education and engagement elements to further train undergraduate and graduate students. A 'bottom-up" crowd-sourcing approach to forecasting was guided by more experienced forecasters working with graduate students to produce the daily forecasts (Fig. 12). The crowd-sourcing enabled equitable contributions from 22 people representing 9 institutions, from second-year undergraduates who also post-processed dropsonde data to place onto the GTS, to professor emeriti, and included key local knowledge from Swedish and Norwegian scientists. The approach boosted an awareness of new data sources and perspectives. NSF also supported the US participation of 4 undergraduates and 2 professional scientists focused on CAO cloud modeling. The science team also held weekly, online science presentations open to the global public.

A connection to the local community in Kiruna was developed by the NSF NCAR Education, Engagement & Early-Career Development team. Activities included public talks at the local Swedish Institute for Space Physics and Kiruna city library. Learners acquire more knowledge and interest through doing than passively listening (Falk and Dierking 2010; Anderson et al. 2021; Mcleod 2024) and such informal learning was promoted through an open house at Arena Arctica

Accepted for publication in *Bulletin of the American Meteorological Society.* DOI 10.1175/BAMS-D-25-0241.1.

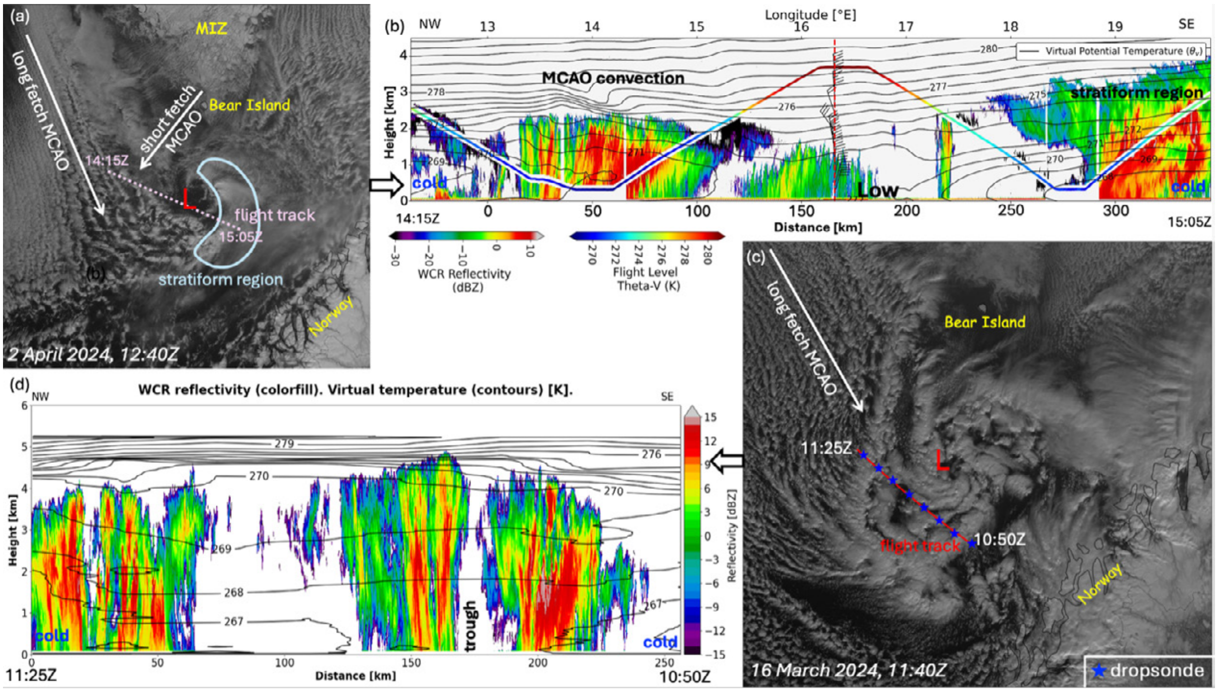

FIG. 11. Two polar lows, a shallow system sampled on 2 April (RF09; panels a-b) and a deeper, more convective polar low on 16 March (RF07; panels c-d). a) Advanced Very High Resolution Radiometer (AVHRR) visible image on 2 April 12:40 UTC (RF09), with C-130 flight track shown from 14:15 UTC to 15:05 UTC (dotted line). b) RF09 2 April 14:15 UTC-15:05 UTC WCR reflectivity with aircraft track shown colored by the virtual potential temperature (θ_v). 15:00 UTC Arome Arctic model θ_v shown interpolated to the transect (black contours). c) 16 March (RF07) VIIRS visible image at 11:40 UTC overlaid with the C-130 flight track from 10:50 UTC to 11:25 UTC (red line) and dropsonde locations (blue stars). d) same as b) but for 16 March (RF07) 10:50 UTC-11:25 UTC.

airport hangar. Here, the public could tour the C-130 aircraft, speak with the CAESAR team, and explore CAESAR science through hands-on demonstrations (Fig. 12). These activities reflect the science of the field campaign in accessible ways for general audiences and emphasize real-world relevance. Hands-on activities were further conducted at "pop-up" tables in the local tourism office and a community space in Kiruna.

Digital media can also promote interest in science careers, and provide audiences with insight into authentic science research (Wyss et al. 2012; Stamer et al. 2020). The Arctic's visual beauty and the CAESAR team's dynamism provided material for compelling videos. These media pieces

Accepted for publication in *Bulletin of the American Meteorological Society.* DOI 10.1175/BAMS-D-25-0241.1.

FIG. 12. Left: Kiruna citizens lining up to tour the C-130 during the open house at the Kiruna Arena Arctica airport hangar. Right: A day in the life of the forecasting/debriefing room. Forecasting and flight planning benefitted from the broad range of backgrounds represented, including senior and early-career scientists and students encompassing a wide range of science expertise and experience, research staff comprised of communication and software experts, instrumentation technicians and education specialists, and the pilots and aircraft maintenance personnel. Photo credits: DZ (left) and GM (right)

showcase the complexity of our planet, and develop humility on the fragility of the Arctic coupled system. We invite the reader to view the videos available on the Science of CAESAR, CAESAR: Life on an Arctic Field Project (both official selections at the 2024 Polar Film Fest), as well as the CAESAR Science Team, at `https://edec.ucar.edu/public/field-projects/caesar`, and a slide show of microphysical imagery set to a music background at `https://www.youtube.com/watch?v=DOptMfkGdA8`.

11. Conclusions

The March 16 2024 (RF07) case study sampled a boundary layer in initially clear-skies that nevertheless still indicated anthropogenic influences, with leads upstream furthermore establishing cloud streets even over 100% sea ice. This challenges the $H1$ assumption that a 'pristine' upstream boundary condition can be easily generalized for the subsequent cloud evolution. Another case study, of closed cells evolving into open cells under weak wind shear, strong surface fluxes, and high initial aerosol loading, occurring on 29 February 2024 (RF02), occurs enough downstream of the Arctic ice that the influence of the initial stratification may no longer be critical to the transition to lower cloud fractions (Ephraim et al. 2026), disproving $H1$. Rather, more in line with $H2$, the cloud transition is clearly linked to precipitation supported by a deepening boundary layer able to produce drizzle-sized drops, confirming $H3$. In both cases, the presence of super-cooled liquid preceeds ice production (consistent with $H4$), although the time scale for the initial ice production

Accepted for publication in *Bulletin of the American Meteorological Society*. DOI 10.1175/BAMS-D-25-0241.1.

in the March 16 case is fast enough that no liquid was detected at flight-level at first encounter with cloud. This case is still consistent with the canonical view that Arctic CAO cloud genesis begins as a thin, super-cooled liquid-only cloud, before transitioning to mixed-phase, supported by statistically-robust satellite analyses (Murray-Watson and Gryspeerdt 2024; Carlsen and David 2022), other aircraft campaigns (Schirmacher et al. 2024) and ground-based analyses (de Boer et al. 2011), although Fig. 9e displaces the notion that all-liquid clouds are easily sampled prior to glaciation.

For the 29 February case, high CCN concentrations can be attributed primarily to advected anthropogenic emissions, as opposed to ocean emissions, contradicting $H4$, but most BL aerosols can otherwise typically be attributed to the ocean (Cai et al. 2026). The analysis of two polar lows confirms $H5$, in that both the shallow polar low sampled extensively on 2 April (RF09) and the deep, purely convective polar low of 16 March (RF07) were driven by strong surface heat fluxes mixed into a deepening BL by moist convection and associated with an upper-level positive potential vorticity anomaly during their formation.

Not all CAESAR CAO cases have been observationally analyzed yet. Regardless, it is becoming clear that not all CAOs are alike, begging deeper observational dives and constrained modeling to establish the sensitivity to the environmental and aerosol conditions reflected in the CAESAR hypotheses. One goal of this paper is to encourage this activity.

The March 16 2024 (RF07) case in particular succeessfully documented the complete evolution from cloud-free airmass to multi-cellular cloud complexes and polar lows over the open ocean-through its dropsonde density, remote sensing and in situ measurements. Such measurements help connect MOSAiC measurements made over the central Arctic pack ice from a drifting platform to the measurements from European-led campaigns through remote sensing (e.g., HALO-AC^3; Wendisch et al. 2024; Schirmacher et al. 2024) or further south (e.g., ACAO; Raif et al. 2024; Aragon et al. 2025) and expand the range of CAOs characterized within multiple campaigns (Table 1). This is also valuable as more becomes known about the differences in the aerosol and environmental conditions of the high-latitudes in the northern versus southern hemispheres. The remote sensing datasets hold further promise of extending information on the ice-liquid phase partitioning for both cloud and precipitation.

Accepted for publication in *Bulletin of the American Meteorological Society*. DOI 10.1175/BAMS-D-25-0241.1.

The CAESAR campaign did not include a dedicated separate modeling component, with ongoing efforts preparing the datasets to ease their utility for model assessment and incorporation into process studies (Table A2). For example, the merged aerosol distribution decribed within-Cai et al. (2026) suggests sea-spray production is likely underestimated within Goddard Earth Observing System composition forecasts. Anticipated simulations also examine representative CAO cases using the Weather Research and Forecasting model, the Distributed Hydrodynamic Aerosol-Radiation-Microphysics Application (e.g., Tornow et al. 2025a) and single-column models (e.g., Hartung et al. 2018; Karalis et al. 2025), including within a Lagrangian framework,. These experiments span a range of initial and boundary conditions, horizontal grid spacings from convection-permitting to large-eddy scales, and diverse physics parameterizations. Combined with sensitivity experimentation, the anticipated modeling framework supports rigorous testing of CAESAR's hypotheses on air-sea interactions, boundary layer evolution, mesoscale cloud organization, cloud and precipitation microphysics, aerosol origins and impacts, and polar-low development.

Acknowledgments. The authors gratefully acknowledge support and engagement from the US National Science Foundation for the CAESAR field campaign, and specifically Nick Anderson, Yu Gu and Subhashree Mishra and NCAR EOL Director Allison McCominskey. PZ and SE acknowledge financial support from NSF AGS-2150848, BG from AGS 2151329, MP, LC and SM through AGS-2412409, EW, AR and JS through AGS-2150812, GM, NA, AD, QN, SP, ZX through AGS-2150774; YW, AC, SG, BL through AGS-2317166; RP, KB, CM, and RP through AGS-2150040; ZW and MM through AGS-2151075. The National Center for Atmospheric Research is a major facility sponsored by the National Science Foundation under Cooperative Agreement 1852977. JDD acknowledges the support of the NRL Base Program, Air-Sea-Ice Interactions and Intense Polar Lows, PE-0601153N, as well as the support of the Office of Naval Research PE-0602435N. HS (and AS) acknowledge European Research Council funding within the H2020 project ISLAS (grant no. 773245). ROD and TC acknowledge support from the European Research Council through Consolidator Grant 101045273 (STEP-CHANGE), EU-HORIZON-WIDERA-2021 Grant 101079385 (BRACE-MY) and the University of Oslo's Cold Climate Container Facilities. We further gratefully acknowledge Trude Storelvmo's contributions to the proposal development and complementary data collection.

Accepted for publication in *Bulletin of the American Meteorological Society.* DOI 10.1175/BAMS-D-25-0241.1.

The authorship list attempts to recognize all major technical and scientific contributions to the CAESAR campaign. The 3 investigators who conceived and led CAESAR are listed first, followed by the 9 other principal investigators. The second alphabetized list is of those who made major contributions to the organization and execution of the campaign, and subsequently an alphabetic list is of investigators and collaborators who contributed to more individual aspects of the campaign, including execution, instruments, and datasets. This overview was mostly written by the lead author. Much thanks are due to the pilots (Bo LeMay, Stephen Jude, Brent Markowski, Ed Proulx, Joe LoRusso, Missy Martin), flight engineers (Carlos Molinari, Aaron Steinbach), flight technicians (Ivana Vu, Richard Freeman, Dave Allbee, Aaron Gunlock, and Edward Kosciuch) and other mechanics and technicians who supported the C-130 aircraft, along with the 'Tank Tiger' team. A special thanks to Kiruna airport manager Andreas Fredriksson, Hangar Manager Kurt Mäki, and Uwe Raffalski from the Swedish Space Institute for their support, assistance and advice, and the Swedish Air Forces for their logistical leadership and cooperation.

Data availability statement. The full CAESAR Field Data Archive, containing all CAESAR instrument data and then some, is available at `https://data.eol.ucar.edu/project/CAESAR`. Daily passive microwave sea ice concentrations for Fig. 1 are from a climate data record constructed by the National Snow and Ice Data Center (NSIDC), at a spatial resolution of 25 km by 25 km (`https://nsidc.org/data/g02202/versions/4`).The NSIDC median 1981-2021 sea ice extents are available at `https://nsidc.org/data/g02135/versions/3t`. Regional trends in sea ice extent are derived from N_Sea_Ice_Index_Regional_Monthly_Data_G02135_v3.0.xlsx.

APPENDIX

Measurement Specifics and Ancillary Information

The full instrument suite and prominent individual instrument details are listed in Table A1. Table A2 lists the aerosol, cloud, and remote sensing-derived value-added products along with animated movies available for each flights. Table A3 lists additional datasets from satellites and models collected specifically for CAESAR.

Three inlets controlled the aerosol and gas intakes on the plane. The High-Performance Instrumented Airborne Platform (HIAPER) Modular Inlet (HIMIL; Craig et al. 2013) serviced both cloud condensation nuclei counters, and the Ultra-High Sensitivity Aerosol Spectrometer (UH-

Accepted for publication in *Bulletin of the American Meteorological Society.* DOI 10.1175/BAMS-D-25-0241.1.

SAS), as well as the gas measurements of O_3, CO and N_2O. The forward-facing Solid Diffuser Inlet (SDI; Huebert et al. 2004), for which isokinetic flow conditions at the inlet tip minimize loss of aerosol particles passing from the atmosphere into the aircraft cabin, provided the sampling for the Scanning Mobility Particle Sizer (SMPS) and Single Particle Soot Photometer (SP2). A submicron aerosol inlet (SMAI; Craig et al. 2013) was used for the condensation nuclei (CN) counter. The Counterflow Virtual Impactor (CVI; Noone et al. 1988) collected data in-cloud on liquid and ice particles, after which the particles were evaporated/sublimated, the water vapor analyzed for their isotopes, and the aerosols ingested into the CFDC for INP characterization. The aerodynamic cut size of the SDI is 3-5 μm, that of the SMAI is $\sim$ 3 μm, and that of the HIMIL is $\sim$ 1 μm. The PCASP probe was wing-mounted with its own inlet (see Appendix D of Snider et al. 2017).

a. In situ gas and state parameters

A radome gust probe provided three-dimensional in situ wind observations up to 25 Hz. This is complemented by 25 Hz temperature measurements from an unheated sensor, with a heated sensor providing slower 1 Hz temperature measurements. Pressure measurements are at 25 Hz.

Measurements of the CO, O_3 and N_2O gases were made by a Picarro analyzer. One isotopic Picarro analyzer sampled water vapor in cloud-free conditions. A second isotopic analyzer sampled behind the CVI to deduce the isotope ratios of condensate in liquid, ice, and mixed-phase clouds. A cryocooler (Seidl 2025) froze out moisture contained in the CVI inlet air stream for later laboratory analysis.

Two other instruments besides the Picarro isotope analyzer sampled water vapor. A vertical cavity surface emitting laser (VCSEL) provides fast-response (25 Hz) water vapor mixing ratio measurements, while a chilled-mirror hygrometer provides slower-response but more robust water vapor mixing ratios. Of the three measurements, the isotope analyzer is most precise, while the chilled-mirror is least prone to icing (not shown here).

CAESAR supported the first C-130 deployment of the smaller Vaisala NRD41 dropsondes developed by NCAR. The 116 successfully-released dropsondes (112 with wind data) include 25 experimental sondes with sea surface temperature sensors, accelerometers, and new GPS receivers. Their datasets were placed upon the Global Telecommunications System (GTS) to allow assimilation by forecasting centers, though the transmission to GTS was not necessarily real-time.

Accepted for publication in *Bulletin of the American Meteorological Society.* DOI 10.1175/BAMS-D-25-0241.1.

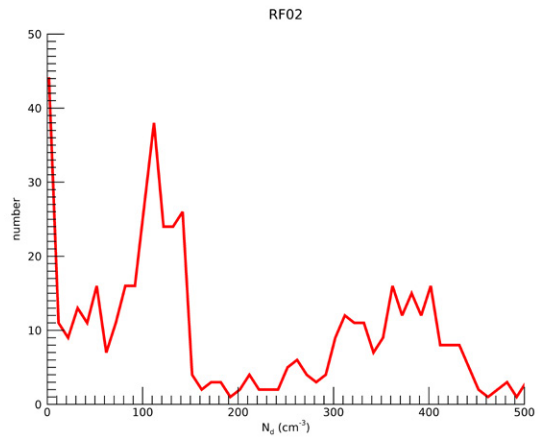

FIG. A1. Cloud droplet number concentration frequency histogram for the 29 February 2024 RF02 flight, derived from the CDP. This flight sampled the highest N_d of the campaign, with the air mass originating in part from Siberia (Ephraim et al. 2026).

b. Aerosols

The five aerosol sensors spanning diameters from 10 nm to 0.5 mm (Cai et al. 2026) include: a CN counter, the SMPS (~ 0.010 μm- ~0.175 μm), UHSAS (0.07 μm-1.1 μm), the Passive Cavity Aerosol Spectrometer Probe (PCASP) measuring up to 3 μm diameter, and the scattering channel of the SP2 (0.2μm-0.5 μm). Cloud condensation nuclei (CCN) sizing and number concentrations were measured by 2 counters, with the DMT-CCN counter operating at 1Hz and the Wyoming CCN (W-CCN) instrument taking a sample every 30 seconds. Both instruments operated at a constant 0.4% supersaturation: scanning through a range of supersaturations on the typically ~ 5 minute-long surface levels would otherwise reduce the data sample size.

Online INP measurements measured by the Colorado State University (CSU) Continuous Flow Diffusion Chamber (CFDC; Moore et al. 2024; Patnaude et al. 2025) were amplified by the first airborne deployment of an aerosol concentrator, resulting in enhancement factors for supermicron aerosol of up to 50x. These were done at instrument temperatures between -18 °C to -28 °C. Filters collected during flight by the CSU ice spectrometer (IS; Hill et al. 2016; Barry et al. 2025) received destructive treatments of portions of particle suspensions prior to freezing tests, providing insight into different compositions. INP samples collected by U of Oslo near the town of Napp on the

Accepted for publication in *Bulletin of the American Meteorological Society.* DOI 10.1175/BAMS-D-25-0241.1.

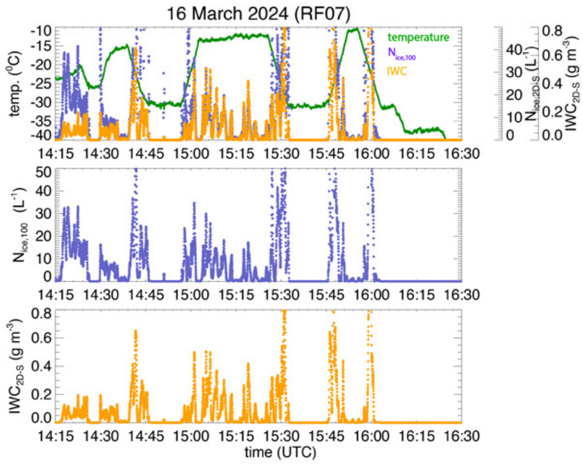

Fig. A2. Top panel: March 16 (RF07) 14:15 UTC-16:30 UTC temperature (green), 2D-S particle number concentration for sizes > 100 μm ($N_{ice,100}$) purple) and 2D-S ice water content (IWC) estimate (orange). For greater clarity, $N_{ice,100}$ and IWC are shown again separately in the middle and bottom panels. Time span corresponds to that in Fig. 8.

Lofoten peninsula, Norway, use a similar technique (Gjelsvik et al. 2025) and extend measurements to warmer temperatures.

c. Cloud Microphysics

A King hot-wire probe provides a bulk liquid water content (LWC), and, important for liquid and ice phase discrimination, a Nevzorov hot-wire probe provided total and LWC measurements. A Rosemount icing detector provdes further information on the presence of supercooled water. The four in situ cloud microphysics sizing probes are the Cloud Droplet Probe (CDP), spanning 2 μm to 50 μm, the Two-Dimensional Cloud Probe (2D-C, 25-1600 μm), the Fast-response Two-Dimensional Stereo Probe (F2D-S or 2D-S, 10-1280 μm) and High Volume Precipitation Sensor (HVPS-3, 150 μm-19 mm). All in situ cloud probes are equipped with anti-shatter tips, and inter-arrival time dependencies are evaluated to reduce remaining shattering artefacts. Archived data may exclude the first 1-2 bins from these full measurement ranges. The 2D-C cloud probe was primarily included to be redundant with the 2D-S. The 2D-S is preferable because of its higher resolution (10 μm/pixel versus 25μm/pixel), more diodes (128 instead of 64) and faster electronics

Accepted for publication in *Bulletin of the American Meteorological Society.* DOI 10.1175/BAMS-D-25-0241.1.

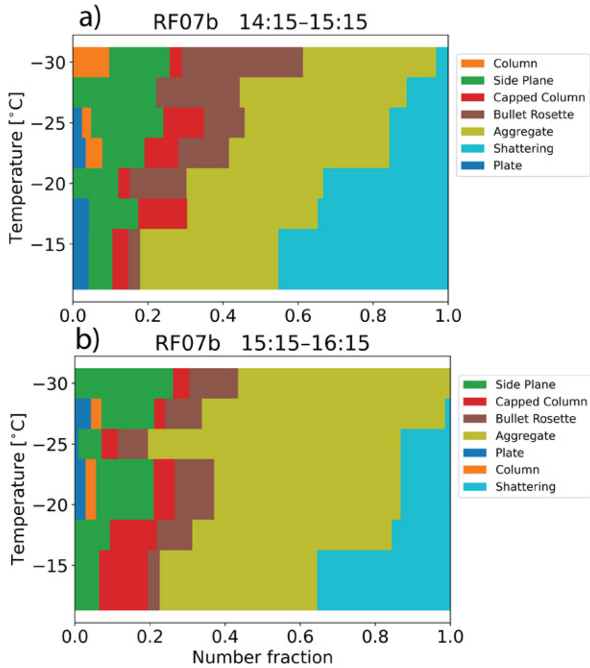

FIG. A3. An objective PHIPS habit classification algorithm under development applied to 16 March (RF07) a) 14:15-15:15 UTC and b) 15:15-16:15 UTC imagery from both sub-cloud and in-cloud legs. Riming is not considered.

providing more counting statistics. The 2D-S and HVPS-3 are also hermetically sealed whereas the 2D-C is not.

The Particle Habit Imaging and Polar Scattering (PHIPS) probe bases the habit detection on bright-field stereo-microscopic imaging of the cloud particles from two viewing angles separated by 120°, with an optical resolution of 6 μm. The three-dimensional imagery from the Holographic Detector for Clouds v.2 (HOLODEC-II) probe has been condensed into size, shape and spatial distribution information within a 15 cm^3 volume. The HOLODEC-II's automated processing has been improved, generating netcdf files at 1 Hz resolution of size, shape, and spatial distribution.

F2D-S and HVPS-3 size sampling overlap and are available merged, with 1200 μm chosen as the threshold to switch between the probes for deriving an integrated size distribution. A more sophisticated phase discrimination approach is also currently underway using the fraction of spherical particles for sizes > 50 μm from the 2D-S, the total 2D-S concentration, the 2D-S median

Accepted for publication in *Bulletin of the American Meteorological Society.* DOI 10.1175/BAMS-D-25-0241.1.

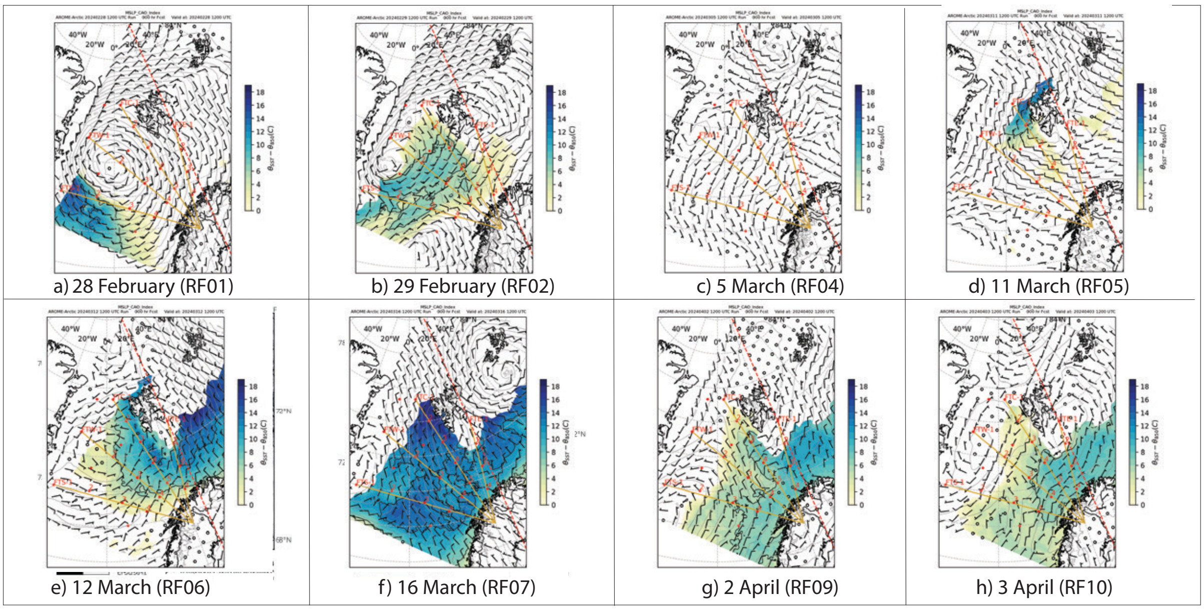

Fig. A4. Arome-Arctic model depictions of the lower tropospheric instability, sea level pressure and surface winds for a) 28 February (RF01), b) 29 February (RF02), c) 5 March (RF04), d) 11 March (RF05), e) 12 March (RF06), f) 16 March (RF07), g) 2 April (RF09) and h) 3 April (RF10), all of 2024, at 12 UTC. Red dashed lines indicate lines along with curtain plots were also generated

mass diameter, and the concentration of HVPS particles with diameter > 1000 μm (Schima et al. 2022).

Liquid water content (LWC) from the HOLODEC integrated dropsize distributions (DSDs) compared well to the CDP_{in} integrated DSDs and both were within 0.1 gm^{-3} of the bulk hot-wire King and Nevzorov LWC measurements. The ice-sensitive bulk water probes (CVI, and Nevzorov TWC), also compared within the instrument error. Larger differences between them can often be attributed to high concentrations of particle sizes outside the range of the probe's collection efficiency.

d. Remote Sensors

The 95-GHz Wyoming Cloud Radar (WCR) measures reflectivities and Doppler velocities both above and below the plane as well as at a slant. Level-2 processing combines the upward- and downward-pointing WCR measurements. The downward-pointing 35-GHz K-band Profiling Radar

Accepted for publication in *Bulletin of the American Meteorological Society*. DOI 10.1175/BAMS-D-25-0241.1.

(KPR) is more sensitive to the larger ice precipitation. The upward-pointing 355-nm wavelength depolarization backscatter Wyoming Cloud Lidar (WCL) establishes cloud base and sub-cloud precipitation phase in addition to aerosol vertical structure. Two narrowband infrared radiometers (Haggery et al. 2003)) sense the surface and cloud temperatures. Broadband radiometers provide the short- and longwave fluxes.

e. Value-added Parameters, Satellite and Model Parameters

A merged ice particle size distribution from two optical array probes with overlapping measurements is already available. A preliminary phase for particles with diameters > 35 and 100 μm is determined based on a sphericity threshold of 0.7 applied to F2D-S imagery, following Korolev and Isaac (2003). From these, calculated ice water contents (IWC) rely on the Brown and Francis (1995) mass-size parameterization.

Visible and infrared satelite imagery and derived cloud products (cloud phase, cloud optical depth, cloud top effective radius, cloud top height and pressure, cloud base height and pressure) are available at 3-hourly resolution. Instantaenous microwave satellite-derived (MAC-LWP Elsaesser et al. 2017) is available at 0.25° resolution for the entire campaign. Arome-Arctic model data and imagery are also archived, with example figures for each flight day shown in Fig. A4.

Accepted for publication in *Bulletin of the American Meteorological Society.* DOI 10.1175/BAMS-D-25-0241.1.

TABLE A1. Instrument Description, Specifics, Parameters and Details of Interest. One-second sampling unless otherwise noted. *=PI instrument

Instrument	Description	Specifics	Parameters, Details	flights	doi
cloud in situ					
Fast Two-Dimensional Stereo Probe (F2D-S[0])	particle images	10-1280 μm, 10 μm res.	N^1, IWC[2], $\overline{D}^1$, phase[2]	all	10.26023/NFNP-51FQ-VX00
Cloud Droplet Probe (CDP)	forward scattering probe	2-50 μm, 2 μm res.	N, LWC, $D_{eff}{}^3$	all	10.26023/44NW-3RPN-ZF0B
Two-Dimensional Cloud Probe (2D-C)	particle images	25-1600 μm, 25 μm res.	N, IWC, $\overline{D}$	all	10.26023/44NW-3RPN-ZF0B
King hot-wire Probe	evaporative LWC estimate	±15%, 0.02 g m^{-3} 'dry bias'	LWC	all	10.26023/44NW-3RPN-ZF0B
*Particle Habit Imaging, Polar Scat. Probe (PHIPS)	images, phase	1.62 μm res., 10Hz	D_{max}, A	5-10	10.26023/QFN9-BYX8-BP0H
High Volume Precipitation Sensor (HVPS-3)	precip size distribution	150 μm-19 mm, 150μm res	N, IWC, $\overline{D}$	all	10.26023/N2NM-4PQQ-7H0C
*Nevzorov LWC/TWC probe	hot-wire	mass only	LWC,TWC[4]	all	10.26023/8EEG-TEPB-FF0V
HOLODEC-II	particle holography	12- ~200 μm, 15 cm^3 vol.	N, D[x,y,z], aspect rat.	all	10.26023/46A1-3CP5-T90J
Rosemount Ice Detector (RICE)	voltage	± 0.01 g m^{-3}	ice accumulation	all	10.26023/44NW-3RPN-ZF0B
aerosol in situ					
*Continuous flow diffusion chamber (CFDC)	INP concs.	1-3 minute ave.	-18°C- -32°C instr. temp.	missing 6	10.26023/6DMM-FYWB-RN11
*CSU ice spectrometer	filters	20-60 min	INP @ freezing temp.	all	10.26023/P9VX-CD1Y-4Z03
*U of Oslo INP	imager+aer.>0.5 μm	–	N_i, $N_{aer} > 0.5$ μm	N/A	10.26023/1391-SAXH-QR0M
*Ultra-High Sensitivity Aer. Spec. (UHSAS)	laser-based aerosol sizes	0.07-1.1 μm	10% undersizing	all	10.26023/5VK4-AJ5D-6Q14
*Scanning Mobility Particle Sizer (SMPS)	aerosol sizes	~0.01-0.175 μm	1-minute, N	all	10.26023/M31B-VN13-Q30X
Passive Cavity Aerosol Spec. Probe (PCASP)	aerosol sizing	0.12-3 μm	N	all	10.26023/44NW-3RPN-ZF0B
Cloud Condensation Nuclei (CCN) counter	DMT	CCN conc. (0.4% SS)	N	4-10	10.26023/F164-BWEQ-R40B
*Cloud Condensation Nuclei (CCN) counter	Wyoming	CCN conc. (0.4% SS)	30 sec, N	all	10.26023/66WG-GRGT-K30Z
Condensation Nuclei (CN) counter	0.010-2 μm dia.			all	10.26023/44NW-3RPN-ZF0B
*Single Particle Soot Photometer (SP2)	ref. black carbon	0.2-0.4/0.06-0.8 μm opt./BC	rBC N, mass	all	10.26023/RWTP-W4E0-H30B
remote sensors (profiles except GVR)					
Wyoming Cloud Radar (WCR)	up+down+slant, 95 GHz, -30 dBz sens.	30 m Δz, up+down merged	dBZ, $V_{Dop}{}^5$, winds	all	10.26023/T6HT-YS4S-YX0H
Wyoming Cloud Lidar (WCL)	up-only 355 nm	3.75 m Δz, ~ 1.5 s	I_{back}, depol.[6]	all	10.26023/700K-PK3C-810A
MARLi	down-only Raman	6 m Δz	H_2O, temp., aer., depol.	all	10.26023/GCWK-RWHV-3F0E
Ka-band Precipitation Radar (KPR)	down-only, 0 dBZ sens.	75 m Δz	dBZ, V_{Dop}	all	10.26023/HPAT-ADY8-WB07
*G-band Vapor Radiometer (GVR)	up-only 183.31 GHz ± 1,3,7, 14 GHz	~ 6 sec	LWP, WVP	all	10.26023/36JM-V39N-R408
KT19 infrared radiometer, up+2 down	9.6-11.5 μm radiance	± 0.75°C	surface, cloud temp.	all	10.26023/44NW-3RPN-ZF0B
broadband radiometers, up+down	total short-,longwave	Eppley	broadband radiation	all	10.26023/44NW-3RPN-ZF0B
downward-looking camera	imagery		imagery	all	10.26023/5RXE-Z098-S00
forward-looking camera	imagery		imagery	all	10.26023/VMK7-J8DW-9M0B
gas in situ, state parameters					
trace gases	Picarro	0.5-1 Hz	CO, O_3, N_2O conc.	all	10.26023/44NW-3RPN-ZF0B
water vapor, oxygen isotopes	Picarro	on-off CVI, 4 Hz	H_2O, $\delta^{18}O$, δD	all	10.26023/44NW-3RPN-ZF0B
*water vapor, oxygen isotopes (U Bergen)	cold trap	on CVI	H_2O, $\delta^{18}O$, δD	all	10.5281/zenodo.20722789
vertical cavity surface emitting laser (VCSEL)	25 Hz	open-path laser H_2O abs.	H_2O conc.	all	10.26023/44NW-3RPN-ZF0B
Chilled-mirror	dewpoint temp.	0.1-2 Hz	H_2O conc.	all	10.26023/44NW-3RPN-ZF0B
Unheated temp.	102AL TAT	25 Hz	temperature	all	10.26023/X2W9-12BD-6C0S
Heated temp.	Harco 100009-1 Deiced TAT	1 Hz	temperature	all	10.26023/44NW-3RPN-ZF0B
Pressure	Paroscientific Digiquartz 1000	25 Hz	pressure	all	10.26023/44NW-3RPN-ZF0B
Radome Gust probe	forward port Δp	25 Hz	vertical winds w	all	10.26023/X2W9-12BD-6C0S
Airborne Vertical Atm. Profiling Systems	Vaisala RS41	25 exp. SST, 116 tot.	temp, p, humidity	all	10.26023/4KSV-GMKT-AT0R

[0]also referred to as 2D-S. [1]N: total particle number concentration. [2]IWC: ice water content. All-ice processing estimates mass following Brown and Francis (1995). LWC: liquid water content. $\overline{D}$: mean diameter. [3]D_{eff}: effective diameter. [4]TWC: total water content. IWC=TWC-LWC. all microphysics reported at full measurement range, archived data may exclude first 1-2 bins for which measurement uncertainties are largest. [5]dBZ: radar reflectivity. V_{Dop}: Doppler velocity. [6] I_{back}: backscattered intensity. depol.: depolarization ratio.

Accepted for publication in *Bulletin of the American Meteorological Society.* DOI 10.1175/BAMS-D-25-0241.1.

TABLE A2. Value-Added Products (VAP)[1]

Product	Description	doi
aerosol	CN+SMPS+UHSAS+SP2+PCASP	10.26023/DQFV-MKGR-J608
microphysical	merged 2D-S+HVPS3, 2D-S liquid/ice discrimination, beta	`https://data.eol.ucar.edu/dataset/391197`
remote sensing	merged WCR+WCL+KPR+MARLi,WCL-cloud top,base heights	10.26023/9SGP-MXGP-MA06
camera movies+animated plots	z,p,lon,temp,w,LWC,N_{2DS}, N_{CDP},O_3; MP4, RF 4,5,6,9,10 only	10.26023/NKZ0-AXTJ-TF08

[1] all at 1-sec time resolution, all flights unless noted otherwise

TABLE A3. Additional Datasets

Product	Author	Description	doi
Sat. visible, IR imagery	NASA Langley SatCorps	VIIRS, NOAA-20,21, 2-hr	10.26023/AYFZ-9TZN-4R11
Sat.-derived cloud products	NASA Langley SatCorps	phase, τ, r_{eff}, LWP	10.26023/PVEV-D5RN-490Q
		base/top z/p/temp,flux	10.26023/PVEV-D5RN-490Q
MAC-LWP[1]	GISS	inst. LWP, 0.25° res	10.26023/H7YK-XSBK-TF10
AROME-Arctic model	Norwegian Met Service	12 km res, daily	thredds.met.no/thredds/catalog/aromearcticarchive/catalog.html
flight-day radiosondes	Nor. Met. Serv.	Jan Mayen, Bjørnøya, 2-hr	thredds.met.no/thredds/catalog/ remotesensingradiosonde/2024/catalog.html

[1] MAC-LWP

Accepted for publication in *Bulletin of the American Meteorological Society.* DOI 10.1175/BAMS-D-25-0241.1.

References

Abel, S. J., I. A. Boutle, K. Waite, S. Fox, P. R. A. Brown, and R. Cotton, 2017: The role of precipitation in controlling the transition from stratocumulus to cumulus northern hemisphere cold-air outbreaks. *J. Atmos. Sci.*, **74**, 2293–2314, https://doi.org/10.1175/JAS-D-16-0362.1.

Aemisegger, F., and L. Papritz, 2018: A climatology of strong large-scale ocean evaporation events. Part I: Identification, global distribution, and associated climate conditions. *J. Climate*, **31**, 7287–7312, https://doi.org/10.1175/JCLI-D-17-0591.1.

Aemisegger, F., and J. Sjolte, 2018: A climatology of strong large-scale ocean evaporation events. Part II: Relevance for the deuterium excess signature of the evaporation flux. *J. Climate*, 7313–7336, https://doi.org/10.1175/JCLI-D-17-0592.1.

Alexander, S. P., G. M. McFarquhar, R. Marchand, A. Protat, E. Vignon, G. G. Mace, and A. R. Klekociuk, 2021: Mixed-phase clouds and precipitation in Southern Ocean cyclones and cloud systems observed poleward of 64°s by ship-based cloud radar and lidar. *J. Geophys. Res.*, **126**, https://doi.org/10.1029/2020JD033626.

Anderson, A., E. K. Kollmann, M. Beyer, O. Weitzman, M. Bequette, G. Haupt, and H. Velázquez, 2021: Design strategies for hands-on activities to increase interest, relevance, and self-efficacy in chemistry. *J. Chem. Ed.*, **98**, 1841–1851, https://doi.org/10.1021/acs.jchemed.1c00193.

Aragon, L., J. Crosier, P. Connolly, Y. Huang, P. May, and S. J. Abel, 2025: Characterizing the shape of cloud particle size distributions in high-latitude marine cold-airoutbreaks. *J. Geophys. Res.*, **130**.

Bailey, H., A. Hubbard, E. S. Klein, K.-R. Mustonen, P. D. Akers, H. Marttila, and J. M. Welker, 2021: Arctic sea-ice loss fuels extreme european snowfall. *Nat. Geosci.*, **14**, 283–288, https://doi.org/10.1038/s41561-021-00719-y.

Barry, K. R., T. Hill, S. M. Kreidenweis, P. J. DeMott, Y. Tobo, and J. M. Creamean, 2025: Bioaerosols as indicators of central arctic ice nucleating particle sources. *Atmos. Chem. Phys.*, **25**, 11 919–11 933, https://doi.org/10.5194/acp-25-11919-2025.

Accepted for publication in *Bulletin of the American Meteorological Society*. DOI 10.1175/BAMS-D-25-0241.1.

Bauduin, S., L.Clarisse, C.Clerbaux, D.Hurtmans, and P.-F.Coheur, 2014: IASI observations of sulfurdioxide (SO2) in the boundary layer of Norilsk. *J. Geophys. Res.*, **119**, 4253–4263, https://doi.org/10.1002/2013JD021405.

Baumann, T. M., øO. Skagseth, R. B. Ingvaldsen, and K. A. Mork, 2025: Reduced cooling in the Norwegian Atlantic Slope Current: Investigating mechanisms of change from 30 years of observations. *EGUsphere [preprint]*, https://doi.org/10.5194/egusphere-2025-2854.

Benavent, N., and Coauthors, 2022: Substantial contribution of iodine to Arctic ozone destruction. *Nat. Geosci.*, **15**, 770–773, https://doi.org/10.1038/s41561-022-01018-w.

Biggart, M., and Coauthors, 2026: Secondary ice production within shallow, mixed-phase clouds in cold air outbreaks over the Labrador Sea. *EGUsphere [preprint]*.

Boyer, M., and Coauthors, 2023: A full year of aerosol size distribution data from the central Arctic under an extreme positive Arctic Oscillation: insights from the Multidisciplinary drifting Observatory for the Study of Arctic Climate (MOSAiC) expedition. *Atmos. Chem. Phys.*, **23**, 389–415, https://doi.org/10.5194/acp-23-389-2023.

Brown, P., and P. Francis, 1995: Improved measurements of the ice water content in cirrus using a total-water probe. *J. Atmos. Ocean. Tech.*, **12**, 410–414.

Brümmer, B., 1999: Roll and cell convection in wintertime Arctic cold-air outbreaks. *J. Atmos. Sci.*, **56**, 2613–2636, https://doi.org/10.1175/1520-0469(1999)056,2613:RACCIW.2.0.CO;2.

Cai, L., S. Mahant, E. Weissburg, A. Robertson, J. R. Snider, and M. D. Petters, 2026: Observed aerosol properties and aerosol forecast evaluation in the Arctic region during cold air oubreaks. *Atm. Res.*, **335**, 108 781, https://doi.org/10.1016/j.atmosres.2026.108781.

Carlsen, T., and R. O. David, 2022: Spaceborne evidence that ice-nucleating particles influence high-latitude cloud phase. *Geophys. Res. Lett.*, **49**, https://doi.org/10.1029/2022GL098041.

Chechin, D. G., and M. K. Pichugin, 2015: Cold-air outbreaks over the ocean at high latitudes and associated mesoscale atmospheric circulations: Problems of numerical modelling. *Izv. Atmos. Ocean. Phys.*, **51**, 1034–1050, https://doi.org/10.1134/S0001433815090078.

Accepted for publication in *Bulletin of the American Meteorological Society.* DOI 10.1175/BAMS-D-25-0241.1.

Chellini, G., R. Gierens, and S. Kneifel, 2022: Ice aggregation in low-level mixed-phase clouds at a high arctic site: Enhanced by dendritic growth and absent close to the melting level. *J. Geophys. Res.-Atmos.*, **127**, https://doi.org/10.1029/2022JD036860.

Clarke, A. D., S. R. Owens, and J. Zhou, 2006: An ultrafine sea-salt flux from breaking waves: Implications for cloud condensation nuclei in the remote marine atmosphere. *J. Geophys. Res.*, **111**, 1–14, https://doi.org/10.1029/2005/JD006565.

Clarke, S. J., and Coauthors, 2026: Marine cold-air outbreaks over the Norwegian– Barents and Labrador seas: observational datasets from the ACAO and M-Phase aircraft campaigns. *ESS Open Archive*, https://doi.org/10.22541/essoar.15004594/v1.

Comiso, J. C., P. Wadhams, L. T. Pedersen, and R. A. Gersten, 2001: Seasonal and interannual variability of the odden ice tongue and a study of environmental effects. *J. Geophys. Res.*, **106**, 9093–9116, https://doi.org/10.1029/2000JC000204.

Craig, L., A.Schanot, A. Moharreri, D. Rogers, and S. Dhaniyala, 2013: Design and sampling characteristics of a new airborne aerosol inlet for aerosol measurements in clouds. *J. Atmos. Oceanic Technol.*, **30**, 1123–1135.

Creamean, J., K. Barry, and T. H. et al., 2022: Annual cycle observations of aerosols capable of ice formation in central Arctic clouds. *Nat Commun*, **13**, 3537–3549, https://doi.org/10.1038/s41467-022-31182-x.

Dahlke, S., A. Solbès, and M. Maturilli, 2022: Cold air outbreaks in Fram Strait: Climatology, trends, and observations during an extreme season in 2020. *J. Geophys. Res.*, **127**, https://doi.org/10.1029/2021JD035741.

Dansgaard, W., 1964: Stable isotopes in precipitation. *Tellus*, **16**, 436–468.

Day, J., and Coauthors, 2024: The Year of Polar Prediction site Model Intercomparison Project (YOPPsiteMIP) phase 1: project overview and Arcticwinter forecast evaluation. *Geosci. Model Dev.*, **17**, 5511–5543, https://doi.org/10.5194/gmd-17-5511-2024.

de Boer, G., H. Morrison, M. D. Shupe, and R. Hildner, 2011: Evidence of liquid dependent ice nucleation in high-latitude stratiform clouds from surface remote sensors. *Geophys. Res. Lett.*, **38**, https://doi.org/10.1029/2010GL046016.

Accepted for publication in *Bulletin of the American Meteorological Society*. DOI 10.1175/BAMS-D-25-0241.1.

Dekhtyareva, A., and Coauthors, 2026: Spatially distributed measurements of aerosols and stable isotopes in water vapour and precipitation in coastal Northern Norway during the ISLAS2021 campaign. *Earth Syst. Sci. Data*, **18**, 2573–2607, https://doi.org/10.5194/essd-18-2573-2026.

DeMott, P. J., and Coauthors, 2025: Ice nucleating particle sources and transports between the Central and Southern Arctic regions during winter cold air outbreaks. *Elementa: Science of the Anthropocene*, **13**, https://doi.org/10.1525/elementa.2024.00063.

Dumont, D., 2022: Marginal ice zone dynamics: history, definitions and research perspectives. *Philos Trans A Math Phys Eng Sci*, **380**, https://doi.org/10.1098/rsta.2021.0253.

Elsaesser, G. S., C. W. O'Dell, M. D. Lebsock, R. Bennartz, T. J. Greenwald, and F. J. Wentz, 2017: The Multisensor Advanced Climatology of Liquid Water Path (MAC-LWP). *J. Climate*, **30**, 10 193–10 210, https://doi.org/10.1175/JCLI-D-16-0902.1.

England, M., L. M. Polvani, J. A. Screen, and A. C. Chan, 2025: Minimal arctic sea ice loss in the last 20 years, consistent with internal climate variability. *Geophys. Res. Lett.*, **52**, https://doi.org/10.1029/2025GL116175.

Ephraim, S., and Coauthors, 2025: A new machine learning retrieval of liquid water path optimised for cold air outbreaks using radiometer and radar observations. *J. Atmos. Ocean. Tech.*, **42**, 1299–1316, https://doi.org/10.1175/JTEC-D-24-0132.1.

Ephraim, S., and Coauthors, 2026: A closed-to-open cell mixed-phase cloud transition observed over the nordic seas under high aerosol loading and strong surface fluxes. *EGUsphere [preprint]*, https://doi.org/10.5194/egusphere-2026-2940.

Falk, J. H., and L. D. Dierking, 2010: The 95 percent solution. *Amer. Sci.*, **98**, https://doi.org/10.1511/2010.87.486.

Field, P. R., and Coauthors, 2017: Exploring the convective grey zone with regional simulations of a cold air outbreak. *Q.J.R. Meteorol. Soc.*, **143**, 2537–2555, https://doi.org/10.1002/qj.3105.

Fu, S., X. Deng, M. D. Shupe, and H. Xue, 2019: A modelling study of the continuous ice formation in an autumnal Arctic mixed-phase cloud case. *Atmos. Res.*, **228**, 77–85, https://doi.org/10.1016/j.atmosres.2019.05.021.

Accepted for publication in *Bulletin of the American Meteorological Society*. DOI 10.1175/BAMS-D-25-0241.1.

Geerts, B., and Coauthors, 2022: The COMBLE Campaign: A Study of Marine Boundary Layer Clouds in Arctic Cold-Air Outbreaks. *Bull. Am. Meteor. Soc.*, **103 (5)**, E1371 – E1389, https://doi.org/10.1175/BAMS-D-21-0044.1.

Gjelsvik, A. B., R. O. David, T. Carlsen, F. Hellmuth, S. Hofer, Z. McGraw, H. Sodemann, and T. Storelvmo, 2025: Using a region-specific ice-nucleating particle parameterization improves the representation of Arctic clouds in a global climate model. *Atmos. Chem. Phys.*, **25**, 1617–1637, https://doi.org/10.5194/acp-25-1617-2025.

Gong, X., and Coauthors, 2023: Arctic warming by abundant fine sea salt aerosols from blowing snow. *Nat. Geosci.*, **16**, 768–774.

Grzegorczyk, P., S. Yadav, F. Zanger, A. Theis, S. K. Mitra, S. Borrmann, and M. Szakáll, 2023: Fragmentation of ice particles: laboratory experiments on graupel–graupel and graupel–snowflake collisions. *Atmos. Chem. Phys.*, **23**, 13 505–13 521, https://doi.org/10.5194/acp-23-13505-2023.

Haggery, J. A., J. A. Maslanik, and J. A. Curry, 2003: Heterogeneity of sea ice surface temperature at SHEBA from aircraft measurements. *J. Geophys. Res.*, **108**, 8052–, https://doi.org/10.1029/2000JC000560.

Hartmuth, K., H. Wernli, and L. Papritz, 2024: Characteristics and dynamics of extreme winters in the barents sea in a changing climate. *EGUsphere [preprint]*, https://doi.org/10.5194/egusphere-2024-878.

Hartung, K., G. Svensson, H. Struthers, A.-L. Deppenmeier, and W. Hazeleger, 2018: An EC-Earth coupled atmosphere–ocean single-column model (AOSCM.v1EC-Earth3) for studying coupled marine and polar processes. *Geosci. Model Dev.*, **11**, 4117–4137, https://doi.org/10.5194/gmd-11-4117-2018.

Herrmann, M., L. Cao, H. Sihler, U. Platt, and E. Gutheil, 2019: On the contribution of chemical oscillations to ozone depletion events in the polar spring. *Atmos. Chem. Phys.*, **19**, 10 161–10 190, https://doi.org/10.5194/acp-19-10161-2019.

Accepted for publication in *Bulletin of the American Meteorological Society.* DOI 10.1175/BAMS-D-25-0241.1.

Hill, T. C., P. J. DeMott, Y. Tobo, J. Fröhlich-Nowoisky, B. Moffett, G. Franc, and S. M. Kreidenweis, 2016: Sources of organic ice nucleating particles in soils. *Atmos. Chem. Phys.*, **16**, 7195–7211.

Hu, Y., and Coauthors, 2023: Vertical structure and ice production processes of shallow convective postfrontal clouds over the Southern Ocean in MARCUS. Part I: Observational study. *J. Atmos. Sci.*, **80 (5)**, 1285 – 1306, https://doi.org/10.1175/JAS-D-21-0243.1.

Huang, X., P. R. Field, B. J. Murray, D. P. Grosvenor, F. van den Heuvel, and K. S. Carslaw, 2025: Different responses of cold-air outbreak clouds to aerosol and ice production depending on cloud temperature. *EGUsphere [preprint]*, https://doi.org/10.5194/egusphere-2024-4070.

Huebert, B. J., and Coauthors, 2004: PELTI: Measuring the passing efficiency of an airborne low turbulence aerosol inlet. *Aer. Sci. Tech.*, **38**, 803–826, https://doi.org/10.1080/027868290500823.

Jimenez, C., and Coauthors, 2025: Life cycle studies and liquid-phase characterization of Arctic mixed-phase clouds: MOSAiC 2019–2020 results. *Atmos. Chem. Phys.*, 12 955–12 981, https://doi.org/10.5194/acp-25-12955-2025.

Jonas, C., and Coauthors, 2026: Detection of ozone recovery in the arctic from ground-based measurements. *EGUsphere [preprint]*, https://doi.org/10.5194/egusphere-2025-6473.

Juliano, T. W., C. P. Lackner, B. Geerts, B. Kosović, L. Xue, P. Wu, and J. Olson, 2024: Simulating mixed-phase open cellular clouds observed during COMBLE: Evaluation of parameterized turbulence closure. *J. Geophys. Res.*, **129**, https://doi.org/10.1029/2024JD040889.

Juliano, T. W., and Coauthors, 2026: The Cold-Air Outbreaks in the Marine Boundary Layer Experiment model-observation intercomparison project (COMBLE-MIP), Part I: Model specification, observational constraints, and preliminary findings. *EGUsphere [preprint]*, https://doi.org/10.5194/egusphere-2025-6217.

Karalis, M., G. Svensson, M. Wendisch, and M. Tjernström, 2025: Lagrangian single-column modeling of arctic air mass transformation during HALO-*AC3*. *Atmos. Chem. Phys.*, **25**, 13 177–13 198, https://doi.org/10.5194/acp-25-13177-2025.

Kirbus, B., J. Chylik, A. Ehrlich, S. Becker, M. Scha¨fer, R. Neggers, and M. Wendisch, 2023: Analysis of an arctic cold air outbreak during autumn and related air mass transformations

Accepted for publication in *Bulletin of the American Meteorological Society*. DOI 10.1175/BAMS-D-25-0241.1.

forced by surface changes and advection in higher altitudes. *Elem. Sci. Anth.*, **11**, https://doi.org/10.1525/elementa.2023.00079.

Knudsen, E. M., and Coauthors, 2018: Meteorological conditions during the ACLOUD/PASCAL field campaign near svalbard in early summer 2017. *Atmos. Chem. Phys.*, **18**, 17 995–18 022, https://doi.org/10.5194/acp-18-17995-2018.

Kornhuber, K., and G. Messori, 2023: Recent increase in a recurrent pan-atlantic wave pattern driving concurrent wintertime extremes. *Bull. Amer. Meteor. Soc.*, **104**, https://doi.org/10.1175/BAMS-D-21-0295.1.

Korolev, A., and G. Isaac, 2003: Roundness and aspect ratio of particles in ice clouds. *J. Atmos. Sci.*, **60**, 1795–1808, https://doi.org/10.1175/1520-0469(2003)060⟨1795:RAAROP⟩2.0.CO;2.

Korolev, A., and T. Leisner, 2020: Review of experimental studies of secondary ice production. *Atmos. Chem. Phys.*, **20**, 11 767–11 797, https://doi.org/10.5194/acp-20-11767-2020.

Korolev, A., and J. Millbrandt, 2022: How are mixed-phase clouds mixed? *Geophys. Res. Lett.*, **49**, https://doi.org/10.1029/2022GL099578.

Lackner, C., B. Geerts, T. Juliano, L. Xue, and B. Kosovic, 2023a: Vertical structure of clouds and precipitation during Arctic cold-air outbreaks and warm-air intrusions: Observations from COMBLE. *J. Geophys. Res.*, **128**, https://doi.org/10.1029/2022JD038403.

Lackner, C., B. Geerts, Y. Wang, T. Juliano, L. Xue, B. Kosović, and D. Turner, 2023b: Insights into the relation between vertical cloud structure and dynamics of three polar lows: Observations from COMBLE. *Q. J. Roy. Meteor. Soc.*, **149**, 2992–3013.

Mace, G. G., A. Protat, and S. Benson, 2021: Mixed-phase clouds over the Southern Ocean as observed from satellite and surface based lidar and radar. *J. Geophys. Res.*, **126**, https://doi.org/10.1029/2021JD034569.

Mages, Z., P. Kollias, Z. Zhu, and E. Luke, 2023: Surface-based observations of cold-air outbreak clouds during the COMBLE field campaign. *Atmos. Chem. Phys.*, **23**, 3561–3574, https://doi.org/10.5194/acp-23-3561-2023.

Accepted for publication in *Bulletin of the American Meteorological Society*. DOI 10.1175/BAMS-D-25-0241.1.

Mateling, M. E., C. Pettersen, M. S. Kulie, and T. S. L'Ecuyer, 2023: Marine cold-air outbreak snowfall in the North Atlantic: A CloudSat perspective. *J. Geophys. Res.*, **128**, https://doi.org/10.1029/2022JD038053.

McCoy, I. L., C. S. Bretherton, R. Wood, C. H. Twohy, A. Gettelman, C. G. Bardeen, and D. W. Toohey, 2021: Influences of recent particle formation on southern ocean aerosol variability and low cloud properties. *J. Geophys. Res.*, **126**, https://doi.org/10.1029/2020JD033529.

McCoy, I. L., R. Wood, and J. K. Fletcher, 2017: Identifying meteorological controls on open and closed mesoscale cellular convection associated with marine cold air outbreaks. *J. Geophys. Res*, **122**, 11,678–11,702, https://doi.org/10.1002/2017JD027031.

McFarquhar, G. M., C. S. Bretherton, R. Marchand, A. Protat, P. DeMott, and S. A. et al., 2021: Observations of clouds, aerosols, precipitation, and surface radiation over the southern ocean: An overview of CAPRICORN, MARCUS, MICRE and SOCRATES. *Bull. Am. Meteor. Soc.*, **102**, E894–E928, https://doi.org/10.1175/bams-d-20-0132.1.

McGinnity, F., Z. Wang, G. Lin, P. Zuidema, B. Geerts, J. Cassano, S. Ephraim, and Y. Chu, 2026: Spatially resolved latent and sensible heat fluxes in the boundary layer of a cold air outbreak using airborne wavelet analysis: A CAESAR case study. *ESS Open Archive Preprint*, https://doi.org/10.22541/essoar.15002448.

Mcleod, S., 2024: Constructivism learning theory & philosophy of education. *Simply Psychology*.

Moore, K. A., and Coauthors, 2024: Characterizing ice nucleating particles over the Southern Ocean using simultaneous aircraft and ship observations. *J. Geophys. Res.*, **129**.

Murray, B. J., D. O'Sullivan, J. D. Atkinson, and M. E. Webb, 2012: Ice nucleation by particles immersed in supercooled cloud droplets. *Chemical Society Reviews*, **41**, 6519–6554, https://doi.org/10.1039/C2CS35200A.

Murray-Watson, R. J., and E. Gryspeerdt, 2024: Air mass history linked to the development of Arctic mixed-phase clouds. *Atmos. Chem. Phys.*, **24**, 11 115–11 132, https://doi.org/10.5194/acp-24-11115-2024.

Accepted for publication in *Bulletin of the American Meteorological Society*. DOI 10.1175/BAMS-D-25-0241.1.

Newman, E., B. Geerts, J. D. Doyle, C. Grasmick, P. Zuidema, S. Ephraim, and Z. Wang, 2025: Airborne observations of the vertical structure of a shallow polar low in the Norwegian Sea. *Mon. Wea. Rev.*, **154**, https://doi.org/10.1175/MWR-D-25-0109.1.

Noone, K. J., J. A. Ogren, J. Heintzenberg, R. J. Charlson, and D. S. Covert, 1988: Design and calibration of a Counterflow Virtual Impactor for sampling of atmospheric fog and cloud droplets. *Aer. Sci. Tech.*, **8**, 235–244, https://doi.org/10.1080/02786828808959186.

Onarheim, I. H., T. Eldevik, L. H. Smedsrud, and J. C. Stroeve, 2018: Seasonal and regional manifestation of arctic sea ice loss. *J. Climate*, **31**, 4917–4932, https://doi.org/10.1175/JCLI-D-17-0427.1.

Papritz, L., and T. Spengler, 2017: A Lagrangian climatology of wintertime cold air outbreaks in the Irminger and Nordic seas and their role in shaping air–sea heat fluxes. *J. Clim.*, **30**, 2717–2737, https://doi.org/10.1175/JCLI-D-16-0605.1.

Pasquier, J. T., and Coauthors, 2022: The Ny-Ålesund Aerosol Cloud Experiment (NASCENT): Overview and First Results. *Bull. Am. Meteor. Soc.*, **103**, E2533 – E2558, https://doi.org/10.1175/BAMS-D-21-0034.1.

Patnaude, R., and Coauthors, 2025: Characteristics of ice nucleating particles from the long-range transport of Saharan dust. *Geophys. Res. Lett.*, **52**.

Pearson, G. R. L., and Coauthors, 2026: Secondary ice production occurs predominantly between -8 c to -3 c in midlatitude winter mixed-phase marine cold air outbreaks. *ESS Open Archive*, https://doi.org/10.2254/essoar.15002290.

Platt, S., and Coauthors, 2022: Atmospheric composition in the European Arctic and 30 years of the Zeppelin Observatory, Ny-Ålesund. *Atmos. Chem. Phys.*, **22**, 3321–3369.

Raatikainen, T., M. Prank, J. Ahola, H. Kokkola, J. Tonttila, and S. Romakkaniemi, 2022: The effect of marine ice-nucleating particles on mixed-phase clouds. *Atmos. Chem. Phys.*, **22**, 3763–3778, https://doi.org/10.5194/acp-22-3763-2022.

Raif, E. N., and Coauthors, 2024: High ice-nucleating particle concentrations associated with arctic haze in springtime cold-air outbreaks. *Atmos. Chem. Phys.*, **24**, 14 045–14 072, https://doi.org/10.5194/acp-24-14045-2024.

Accepted for publication in *Bulletin of the American Meteorological Society*. DOI 10.1175/BAMS-D-25-0241.1.

Rantanen, M., A. Y. Karpechko, A. Lipponen, K. Nordling, O. Hyvärinen, K. Ruosteenoja1, T. Vihma, and A. Laaksonen, 2022: The Arctic has warmed nearly four times faster than the globe since 1979. *Comm. Earth Environ.*, **3**, 168–177, https://doi.org/10.1038/s43247-022-00498-3.

Rodrıguez, J. P., K. Klemm, C. M. Duarte, and V. M. Eguıluz, 2024: Shipping traffic through the Arctic Ocean: Spatial distribution, seasonal variation, and its dependence on the sea ice extent. *iScience*, **27**, https://doi.org/10.1016/j.isci.2024.110236.

Sarkar, M., A. Bailey, P. Blossey, S. P. de Szoeke, D. Noone, E. Q. Meléndez, M. Leandro, and P. Y. Chuang, 2023: Sub-cloud rain evaporation in the North Atlantic winter trade winds derived by pairing isotopic data with a bin-resolved microphysical model. *Atmos. Chem. Phys.*, **23**, 12 671–12 690, https://doi.org/10.5194/acp-23-12671-2023.

Schima, J., and Coauthors, 2022: Characterization of the vertical structure of Southern Ocean boundary layer clouds using airborne radar, lidar and in-situ cloud data: Results from SOCRATES. *J. Geophys. Res.*, **127**, https://doi.org/10.1029/2022JD037277.

Schirmacher, I., S. Schnitt, M. Klingebiel, N. Maherndl, B. Kirbus, A. Ehrlich, M. Mech, and S. Crewell, 2024: Clouds and precipitation in the initial phase of marine cold-air outbreaks as observed by airborne remote sensing. *Atmos. Chem. Phys.*, **24**, 12 823–12 842.

Schulz, H., and Coauthors, 2019: High Arctic aircraft measurements characterising black carbon vertical variability in spring and summer. *Atm. Chem. Phys.*, **19**, 2361–2384, https://doi.org/10.5194/acp-19-2361-2019.

Schäfer, B., R. O. David, P. Georgakaki, J. T. Pasquier, G. Sotiropoulou, and T. Storelvmo, 2024: Simulations of primary and secondary ice production during an arctic mixed-phase cloud case from the Ny-Ålesund Aerosol Cloud Experiment (NASCENT) campaign. *Atmos. Chem. Phys.*, **24**, 7179–7202, https://doi.org/10.5194/acp-24-7179-2024.

Screen, J., and I. Simmonds, 2010: The central role of diminishing sea ice in recent Arctic temperature amplification. *Nature*, **464**, 1334–1337, https://doi.org/10.1038/nature09051.

Screen, J., and Coauthors, 2025: Causes and consequences of Arctic amplification elucidated by coordinated multimodel experiments. *Commun. Earth Environ.*, https://doi.org/10.1038/s43247-025-03052-z.

Accepted for publication in *Bulletin of the American Meteorological Society.* DOI 10.1175/BAMS-D-25-0241.1.

Seethala, C., and Coauthors, 2024: Microphysical evolution in mixed-phase mid-latitude marine cold-air outbreaks. *J. Atmos. Sci.*, **81**, 1725–1747, https://doi.org/10.1175/JAS-D-23-0203.1.

Seidl, A., and Coauthors, 2026: The ISLAS2020 field campaign: Studying the near-surface exchange process of stable water isotopes during the arctic wintertime. *Earth Syst. Sci. Data*, **18 (3)**, 1969–1993, https://doi.org/10.5194/essd-18-1969-2026.

Seidl, A. W., 2025: Profiling the stable isotope signature of water vapour from kinetic fractionation in Arctic conditions. Ph.d. thesis, University of Bergen, Norway, URL https://hdl.handle.net/11250/3187001.

Serreze, M. C., A. P. Barrett, J. C. Stroeve, D. Kindig, and M. M. Holland, 2009: The emergence of surface-based arctic amplification. *Cryosphere*, **3**, 11–19, https://doi.org/10.5194/tc-3-11-2009.

Siew, P. Y. F., Y. Wu, M. Ting, C. Zheng, R. Clancy, N. T. Kurtz, and R. Seager, 2023: Physical links from atmospheric circulation patterns to barents–kara sea ice variability from synoptic to seasonal timescales in the cold season. *J. Climate*, 8027–8040, https://doi.org/10.1175/JCLI-D-23-0155.1.

Smedsrud, L. H., M. Muilwijk, A. Brakstad, E. Madonna, S. K. Lauvset, and C. Spensberger, 2022: Nordic Seas heat loss, Atlantic inflow, and Arctic sea ice cover over the last century. *Rev. Geophys.*, **60**, https://doi.org/10.1029/2020RG000725.

Smith, D. K. E., and Coauthors, 2025: The impact of mixed-phase cloud processes on simulating Southern Ocean clouds and their radiative effect. *J. Geophys. Res.*, **130**, https://doi.org/10.1029/2025JD044452.

Snider, J. R., D. Leon, and Z. Wang, 2017: Droplet concentration and spectral broadening in southeast pacific stratocumulus. *J. Atmos. Sci.*, **74**, 719–749, https://doi.org/10.1175/JAS-D-16-0043.1.

Solomon, A., H. Morrison, O. Persson, M. D. Shupe, and J. Bao, 2009: Investigation of microphysical parameterizations of snow and ice in Arctic clouds during M-PACE through model–observation comparisons. *Mon. Wea. Rev.*, **137**, 3110–3128, https://doi.org/10.1175/2009MWR2688.1.

Accepted for publication in *Bulletin of the American Meteorological Society*. DOI 10.1175/BAMS-D-25-0241.1.

Stamer, I., H. Pönick, F. Tirre, A. Laherto, T. HøOffler, S. Schwarzer, and I. Parchmann, 2020: Development & validation of scientific video vignettes to promote perception of authentic science in student laboratories. *Research in Sci. Techn. Ed.*, **38**, 168–184, https://doi.org/10.1080/02635143.2019.1600491.

Tan, I., and T. Storelvmo, 2019: Evidence of strong contributions from mixed-phase clouds to Arctic climate change. *Geophys. Res. Lett.*, **46**, 2894–2902, https://doi.org/10.1029/2018GL081871.

Tansey, E., R. Marchand, S. P. Alexander, A. R. Klekociuk, and A. Protat, 2023: Southern Ocean low cloud and precipitation phase observed during the Macquarie Island Cloud and Radiation Experiment (MICRE). *J. Geophys. Res.*, **128**, https://doi.org/10.1029/2023JD039205.

Terai, C., Y. Zhang, S. A. Klein, M. Zelinka, J. C. Chiu, and Q. Min, 2019: Mechanisms behind the extratropical stratiform low-cloud optical depth response to temperature in ARM site observations. *J. Geophys. Res.*, **124**, 2127–2147, https://doi.org/10.1029/2018JD029359.

Tornow, F., and Coauthors, 2025a: High accumulation mode aerosol concentration and moderate aerosol hygroscopicity limit impacts of recent particle formation on Northwest Atlantic post-frontal clouds. *Geophys. Res. Lett.*, **52**.

Tornow, F., and Coauthors, 2025b: Measurement report: A survey of meteorological and cloud properties during ACTIVATE's postfrontal flights and their suitability for Lagrangian case studies. *Atmos. Chem. Phys.*, **25**, 5053–5074, https://doi.org/10.5194/acp-25-5053-2025.

von der Lippe, F., T. Carlsen, T. Storelvmo, and R. David, 2026: Shortening of the Arctic cold air outbreak season detected by a phenomenological machine learning approach. *Atmos. Chem. Phys.*, https://doi.org/10.5194/acp-26-1565-2026.

Wahl, S., B. Walter, F. Aemisegger, L. Bianchi, and M. Lehning, 2024: Identifying airborne snow metamorphism with stable water isotopes. *The Cryosphere*, **18**, 4493–4515, https://doi.org/10.5194/tc-18-4493-2024.

Wang, Y., B. Geerts, and Y. Chen, 2016: Vertical structure of boundary layer convection during cold-air outbreaks at barrow, alaska. *J. Geophys. Res.*, **121**, 399–412, https://doi.org/10.1002/2015JD023506.

Accepted for publication in *Bulletin of the American Meteorological Society.* DOI 10.1175/BAMS-D-25-0241.1.

Wendisch, M., B. Kirbus, D. Ori, M. D. Shupe, S. Crewell, H. Sodemann, and V. Schemann, 2025: Observed and modeled Arctic airmass transformations during warm air intrusions and cold air outbreaks. *Atmos. Chem. Phys.*, **25**, 15 047–15 076, https://doi.org/10.5194/acp-25-15047-2025.

Wendisch, M., and Coauthors, 2024: Overview: quasi-Lagrangian observations of Arctic air mass transformations – introduction and initial results of the HALO–(AC)3 aircraft campaign. *Atmos. Chem. Phys.*, **24**, 8865–8892, https://doi.org/10.5194/acp-24-8865-2024.

Whaley, C. H., and Coauthors, 2023: Arctic tropospheric ozone: assessment of current knowledge and model performance. *Atmos. Chem. Phys.*, **23**, 637–661, https://doi.org/10.5194/acp-23-637-2023.

Williams, A. S., and Coauthors, 2024: Aerosol size distribution properties associated with cold-air outbreaks in the Norwegian Arctic. *Atmos. Chem. Phys.*, **24**, 11 791–11 805, https://doi.org/10.5194/acp-24-11791-2024.

Wu, P., M. Ovchinnikov, H. Xiao, C. P. Lackner, B. Geerts, F. Tornow, and G. Elsaesser, 2025: Effect of ice number concentration on the evolution of boundary layer clouds during Arctic marine cold-air outbreaks. *J. Geophys. Res.*, **130**, https://doi.org/10.1029/2024JD041282.

Wyss, V. L., D. Heulskamp, and C. J. Siebert, 2012: Increasing middle school student interest in STEM careers with videos of scientists. *Int. J. Environ. Sci. Educ.*, **7**, 501–522.

Xia, Z., and G. M. McFarquhar, 2024: Dependence of cloud macrophysical properties and phase distributions on environmental conditions over the North Atlantic and Southern Ocean: Results from COMBLE and MARCUS. *J. Geophys. Res.*, **129**, https://doi.org/10.1029/2023JD039869.

Zuidema, P., D. Leon, A. Pazmany, and M. Cadeddu, 2012: Aircraft millimeter-wave passive sensing of cloud liquid water and water vapor during VOCALS-REx. *Atmos. Chem. Phys.*, **12**, 355–369, https://doi.org/10.5194/acp-12-355-2012.

Accepted for publication in *Bulletin of the American Meteorological Society*. DOI 10.1175/BAMS-D-25-0241.1.